Mon. Not. R. Astron. Soc. **366,** 739–757 (2006) doi:10.1111/j.1365-2966.2005.09829.x

The infrared Hourglass cluster in M8★†

J. I. Arias,[1]‡§ R. H. Barbá,[2]¶ J. Maíz Apellániz,[3]|| N. I. Morrell[4]¶ and M. Rubio[5]

[1]*Facultad de Ciencias Astronómicas y Geofísicas, Universidad Nacional de La Plata, Paseo del Bosque S/N, B1900FWA La Plata, Argentina*
[2]*Departamento de Física, Universidad de La Serena, Benavente 980, La Serena, Chile*
[3]*Space Telescope Science Institute, 3700 San Martin Drive, Baltimore, MD 21218, USA*
[4]*Las Campanas Observatory, Carnegie Observatories, Casilla 601, La Serena, Chile*
[5]*Departamento de Astronomía, Universidad de Chile, Casilla 36-D, Santiago, Chile*

Accepted 2005 November 3. Received 2005 August 18; in original form 2005 February 17

ABSTRACT

A detailed study of the Hourglass nebula in the M8 star-forming region is presented. The study is mainly based on recent subarcsec-resolution JHK_s images taken at Las Campanas Observatory and complemented with archival *Hubble Space Telescope* (*HST*) images and long-slit spectroscopy retrieved from the European Southern Observatory Archive Facility. Using the new numerical code CHORIZOS, we estimate the distance to the earliest stars in the region to be 1.25 kpc. Infrared photometry of all the sources detected in the field is given. From analysis of the JHK_s colour–colour diagrams, we find that an important fraction of these sources exhibit significant infrared excess. These objects are candidates to be low- and intermediate-mass pre-main-sequence stars. Based on *HST* observations, the spatial distribution of gas, dust and stars in the region is analysed. A morphological analysis of these images also reveals a rich variety of structures related to star formation (proplyds, jets, bow shocks), similar to those observed in M16 and M42, along with the detection of the first four Herbig–Haro objects in the region. Furthermore, a long-slit spectrum obtained with the New Technology Telescope confirms the identification of one of them (HH 870) in the core of the Hourglass nebula, providing the first direct evidence of active star formation by accretion in M8.

Key words: stars: formation – stars: pre-main-sequence – H II regions – ISM: Herbig–Haro objects – ISM: jets and outflows.

1 INTRODUCTION

The Lagoon nebula (Messier 8 = NGC 6523–6530) is an extended H II region mainly ionized by two O-type stars: 9 Sagitarii [O4 V(f)] and HD 165052 (O6.5 V + O7.5 V). It is embedded within a molecular cloud which extends to the star cluster NGC 6530. This very young open cluster is believed to be the starting point for a sequential star formation process (Lightfoot et al. 1984) which is still active in the region. Within M8's core lies a distinctive bipolar nebula called the Hourglass, a blister-type H II region which has been produced by the O7.5 V star Herschel 36 (Her 36). The Hourglass, which is about 15 arcsec east–west × 30 arcsec north–south in size, is believed to be an ionized cavity in an inhomogeneous clumpy molecular cloud. The Hourglass region also harbours the ultracompact H II region G5.97–1.17 as well as a number of infrared sources, first observed by Allen (1986), which may form a cluster of very young hot stars, analogous to the Orion Trapezium (Allen 1986). Narrow-band optical imaging with the *Hubble Space Telescope* (*HST*) has revealed that G5.97–1.17 could be a young star surrounded by a circumstellar disc that is being photoevaporated by Her 36, similar to the so-called proplyds seen in the Orion nebula (Stecklum et al. 1998). Furthermore, strong H_2 line emission is produced from around the Hourglass, showing a morphology very similar to that of the CO $J = 3$–2 distribution in the region (White et al. 1997; Burton 2002). This fact and the detection of a jet-like feature extending from Her 36 in *HST* images (Stecklum et al. 1995) suggest there might be a molecular outflow in the core of M8 (Burton 2002). Recently, Rauw et al. (2002) reported X-ray emission from Her 36 as well as probably diffuse X-ray emission from the Hourglass region that might reveal a bubble of hot gas produced by the interaction of the stellar wind of Her 36 with the denser part of the molecular cloud.

In this paper, new high-resolution near-infrared images and photometry of the field surrounding the Hourglass are presented and

★Based in part on observations with the National Aeronautics and Space Administration/European Space Agency (NASA/ESA) *Hubble Space Telescope* obtained from the archive at the Space Telescope Science Institute, which is operated by the Association of Universities for Research in Astronomy, Inc., under NASA contract NAS 5-26555.
†Based in part on observations obtained at the European Southern Observatory, La Silla, Chile.
‡E-mail: julia@xeneize.dfuls.cl
§Fellow of CONICET, Argentina.
¶Member of Carrera del Investigador Científico, CONICET, Argentina.
||Affiliated with the Space Telescope Division of the European Space Agency, ESTEC, Noordwijk, the Netherlands.

compared with archival *HST* emission-line images. All these data provide strong evidence that the core of M8 is an important region of active star formation and pre-main-sequence stellar evolution.

2 OBSERVATIONS AND DATA REDUCTION

2.1 Infrared images

J, H and $K_{\rm short}$ ($K_{\rm s}$) images of the Hourglass region were obtained on 1999 September 26, using the near-infrared camera IRCAM, attached to the 2.5-m Du Pont Telescope at Las Campanas Observatory (LCO), Chile. IRCAM was equipped with a NICMOS III 256 × 256 array (Persson et al. 1992) and has a pixel scale of 0.35 arcsec pixel^{-1}. The seeing during the observations was typically of 0.8–0.9 arcsec giving an optimum sampling. In each band, five partially overlapping frames were taken, covering a total area of 135 × 139 arcsec^2 centred approximately at the position of Her 36. The total on-source times were 360 s in $K_{\rm s}$, 500 s in H and 600 s in J. The frames were combined (median-averaged) after being linearized, dark- and sky-substracted, flat-fielded and cleaned of bad pixels, using SQIID processing routines layered in IRAF.[1] Several standard stars selected from Persson et al. (1998) were observed during the night; these fields were reduced following a similar procedure. The combined (final) images of the Hourglass were then shifted to align stars in each frame.

2.2 *HST* Wide Field Planetary Camera 2 Imaging

A partial *HST* Wide Field Planetary Camera 2 (WFPC2) coverage of the Hourglass nebula is available from the public data base. These images include the brightest part of the nebula and the star Her 36, both centred in the Planetary Camera chip. The orientation of the images (position angle = 56.°0919) allows us to cover the west part of the nebula and corresponds to about 2/3 of the field observed in our infrared images. The WFPC2 data set (proposal ID 6227) was obtained on 1995 July 13 and 14, and September 16, using several narrow-band and broad-band filters. These observations were retrieved from the *HST* Archive and processed using the 'on-the-fly' pipeline. In this work, we use images obtained in F487N (Hβ), F656N (Hα), F658N ([N II]) and F673N ([S II]) narrow-band filters, and F547M (v) and F814W (Johnson I) broad-band filters. The filter characteristics are described in the WFPC2 Instrument Handbook. The first steps of data reduction were straightforward, using IRAF and STSDAS tasks to perform cosmic ray cleaning, and integrating the four individual WFPC2 CCD images into a single mosaic. In order to obtain flux-calibrated 'pure nebular' Hβ and Hα images, we followed the procedure given by O'Dell & Doi (1999). A 'pure' Hβ calibrated image was derived from the F487N image, using the F547M images as continuum. A 'pure' Hα calibrated image was obtained from the F656N 'line' image, considering the contamination of [N II] emission lines through the F658N filter, and again using the F547M as continuum image. In the case of the F673N filter used to derive the 'pure' [S II] calibrated emission-line image, the continuum was interpolated between the F547M and F814W images and the zero-points determined by SYNPHOT (Laidler et al. 2005).

[1] IRAF is distributed by the National Optical Astronomy Observatories, operated by the Association of Universities for Research in Astronomy, Inc., under agreement with the National Science Foundation.

2.3 Long-slit echelle spectroscopy

Two long-slit spectra obtained with the European Southern Observatory (ESO) Multimode Instrument (EMMI) on the New Technology Telescope (NTT) were retrieved from the ESO Archive Facility. The spectra were obtained on 2000 July 31 in the REMD (red medium dispersion) configuration with the echelle (10) grating. The order containing Hα and [N II] emission lines was isolated using the filter Ha 596. The detector was a 2048 × 2048 Tek CCD with 24-μm pixels, given a pixel scale of 0.265 arcsec × 0.041 Å and a spatial extent along the slit of 330 arcsec. The spectra were obtained with a position angle of 0°. The total exposure time was 1800 s.

3 RESULTS

Fig. 1 (left-hand panel) shows the $K_{\rm s}$ frame of the field surrounding the Hourglass nebula. Fig. 1 (right-hand panel) is a $JHK_{\rm s}$ colour composite image, produced combining the J (1.25 μ), H (1.65 μ) and $K_{\rm s}$ (2.2 μ) images as blue, green and red channels, respectively. This false-colour picture shows the effects of extinction, the differences in colour of the stars mainly being a result of differences in reddening. This figure confirms the existence of an infrared star cluster around Her 36, as recently reported by Bica et al. (2003).

3.1 Distance

Most previous investigators estimated the distance to NGC 6530 as 1.8 kpc (V_0–M_V = 11.25–11.3; van Altena & Jones 1972; Sagar & Joshi 1978; van den Ancker et al. 1997). A smaller value was however obtained by Kilambi (1977): V_0–M_V = 10.7. More recently, Sung, Chun & Bessell (2000) calculated the distance modulus of several individual stars, finding that some of them gave values near to V_0–M_V = 11.15–11.35, while other early-type stars gave somewhat smaller values (V_0–M_V = 10.5–11). A more robust determination by Prisinzano et al. (2005), considering a sample that reaches down to $V \sim 23$, led to the value of V_0–M_V = 10.48, which means a significantly lower cluster distance of 1.25 kpc. This distance determination is based on more complete colour–magnitude (CM) diagrams, for which it is possible to define the blue envelope of the star distribution with $V > 14$ because of the obscuration effect of the giant molecular cloud, which strongly reduces the detection of background stars at optical wavelengths.

Although this indetermination in the distance to M8 does not change the main conclusions of this paper, we explore the possibility of deriving our own estimate by considering a group of stars around Her 36 with known spectral types. We gathered optical photometry from Sung et al. (2000) and from the Galactic O Star Catalogue (Maíz-Apellániz et al. 2004a), as well as near-infrared photometry from this work or from the Two-Micron All-Sky Survey (2MASS) Point Source Catalogue (PSC; Second Incremental Data Release; Cutri et al. 2000) for Her 36, 9 Sgr (HD 164794), W9 (HD 164816), SCB 182, SCB 325 and SCB 354 (hereafter we use the 'SCB number' to refer to the sources from Sung et al. 2000). For the O-type stars, the adopted spectral types were either obtained from Maíz-Apellániz et al. (2004a) (Her 36, 9 Sgr) or derived from our spectroscopic data (W9). The stars 9 Sgr and W9 are both suspected to be spectroscopic binaries (cf. Mason et al. 1998). While the binary nature of 9 Sgr was recently confirmed by Rauw et al. (2005), we have detected both components in W9, resulting in a spectral classification of O9.5V + B0V, based on our own data. For B-type stars (SCB 182, SCB 325, SCB 354) we adopted the spectral types from van den Ancker et al. (1997).

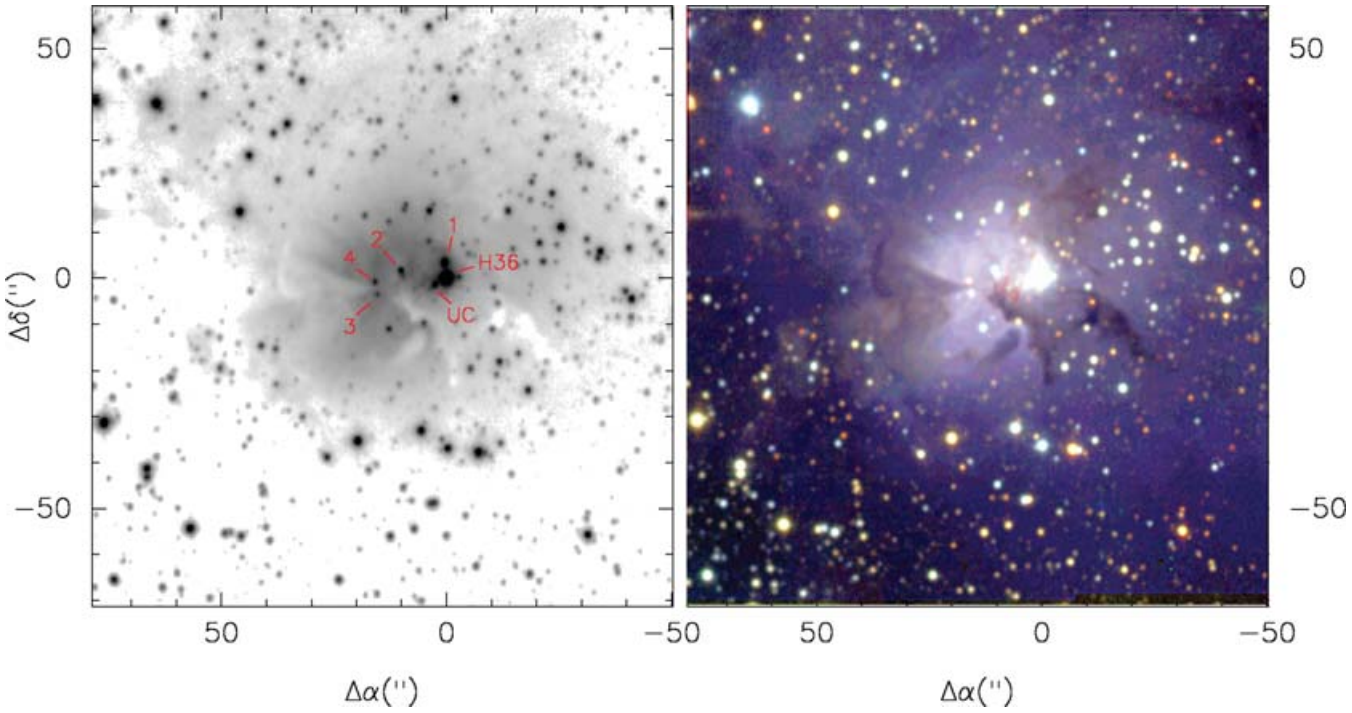

Figure 1. Left-hand panel: K_s image of the field surrounding the Hourglass nebula. Some features of interest are labelled: the ionizing O7.5 V star Her 36 (H36), the infrared sources KS 1–KS 4 and the ultracompact H II region G5.97–1.17 (UC). Right-hand panel: three-colour near-infrared image of the same field. The large majority of sources in this image are not visible at optical wavelengths.

We used the code CHORIZOS developed by Maíz-Apellániz (2004) to derive the individual distance moduli of these stars. CHORIZOS is a code that uses χ^2 minimization to find all models compatible with the observed data set in the model (N-dimensional) parameter space, in our case, broad-band photometry and spectral types. For a complete description of how this method works, see Maíz-Apellániz (2004). We considered TLUSTY (Lanz & Hubeny 2003) atmosphere models and Kurucz[2] models for the spectral energy distribution (SED) of O-type and B-type stars, respectively. Fig. 2 shows the SED corresponding to the best CHORIZOS fit (spectrum) and the synthetic photometry associated with the best SED (stars) for Her 36. The photometric data used for the CHORIZOS fit are also shown in the figure. H and K_s filters were not considered because of the infrared excess of Her 36, which is readily apparent in the plot. Table 1 lists all the compiled quantities and the derived parameters, i.e. the colour excess $E(4405–5495)$ and the ratio of total to selective absorption R_{5495}, which are the monochromatic equivalents to the usual $E(B–V)$ and R_V, respectively (for a detailed explanation, see Maíz-Apellániz 2004), and the distance modulus. The χ^2 values corresponding to the best fit in each case have also been included in the last column. The main source of error comes from the adopted values of the absolute magnitudes. The R_{5495} value is close to the canonical one of 3.1 only for W9; for the rest of the stars, it shows 'anomalous' values. In particular, the value of $R_{5495} = 5.36$ derived for Her 36, which represents one of the highest R_V values known (cf. Cardelli, Clayton & Mathis 1989), is in excellent agreement with earlier estimations. Besides, as mentioned before, the analysis of its SED using CHORIZOS shows that this star presents an evident infrared excess, which is also apparent in the near-infrared colour–colour (CC) diagram (see Section 3.3).

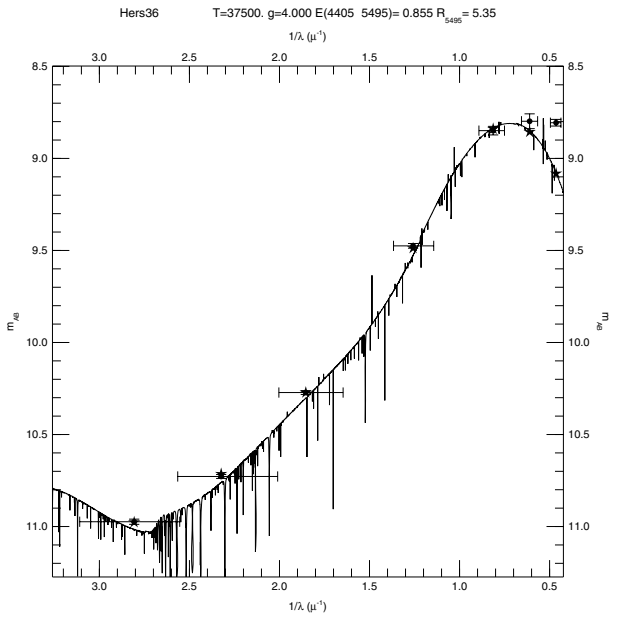

Figure 2. $UBVIJHK_s$ photometry (data with error bars), SED corresponding to the best CHORIZOS fit (spectrum) and synthetic photometry associated with the best SED (stars) for Her 36. For the photometry, vertical error bars display photometric uncertainties and horizontal ones display the approximate extent of the passband. The H and K_s filters were not used for the CHORIZOS fit because of the infrared excess of Her 36, which is readily apparent in the plot.

As also shown in Table 1, the four earliest stars lead to an average distance modulus of nearly 10.5 (1.25 kpc), clearly lower than

[2] See http://kurucz.harvard.edu.

Table 1. Individual distance moduli derived with CHORIZOS for some early-type stars in M8.

Name	Spectral type	V	M_V[a]	$E(4405–5495)$[b]	R_{5495}[b]	A_V	V_0–M_V	χ^2
Her 36	O7.5 V(n)	10.297	-4.80 ± 0.20	0.85 ± 0.01	5.39 ± 0.09	4.60 ± 0.04	10.50 ± 0.20	2.32
9 Sgr	O4 V((f))	5.966	-5.50 ± 0.20	0.32 ± 0.02	3.93 ± 0.25	1.26 ± 0.03	10.21 ± 0.20	1.00
W9	O9.5 V+B0 V	7.089	-4.60 ± 0.20	0.28 ± 0.03	3.33 ± 0.25	0.94 ± 0.07	10.75 ± 0.21	2.34
SCB 182	B2 V	9.953	-2.20 ± 0.20	0.39 ± 0.02	4.50 ± 0.20	1.77 ± 0.04	10.52 ± 0.20	0.90
SCB 325	B7 V	11.552	-0.60 ± 0.20	0.27 ± 0.02	4.09 ± 0.26	1.11 ± 0.04	11.04 ± 0.20	2.75
SCB 354	B7 V	11.922	-0.60 ± 0.20	0.25 ± 0.01	3.79 ± 0.20	0.97 ± 0.03	11.55 ± 0.20	2.11

[a] Values from Walborn (1972, 1973).
[b] $E(4405–5495)$ and R_{5495} are the monochromatic equivalents to $E(B–V)$ and R_V (see Maíz-Apellániz 2004).

that previously adopted by other authors and similar to the value derived by Prisinzano et al. (2005). However, the distance modulus derived for the two B7-type stars is somewhat larger ($\sim$11.3). Such a problem is illustrated in the Hertzsprung–Russell (HR) diagram compiled from the CHORIZOS output, which is shown in Fig. 3. Ellipses indicate the 68 per cent likelihood contour for each star. The main sequence for $5 \log d - 5 = 10.5$ has been marked with a solid line. As seen in the plot, such a distance is compatible with the CHORIZOS output for the four earliest stars but not for the latest two.

We note here that the association of 9 Sgr, located $\sim$3 arcmin to the north-east of Her 36, with the Hourglass region is based not only in a common distance but also in the observed morphology of the gas and dust in the region. Besides a dust 'finger-shape' structure that will be discussed later, the northern part of the nebula seems to be illuminated by this massive star. This is especially evident in the photodissociation regions (PDRs) facing 9 Sgr observed in *HST* images (see Figs 11 and 12 in Section 3.8).

Based on the values derived for the earliest stars, which are systematically smaller than those previously published, we adopt a distance modulus of V_0–$M_V = 10.5$ for the Hourglass region. A possible explanation for the disagreement with the values derived by other authors is considered here.

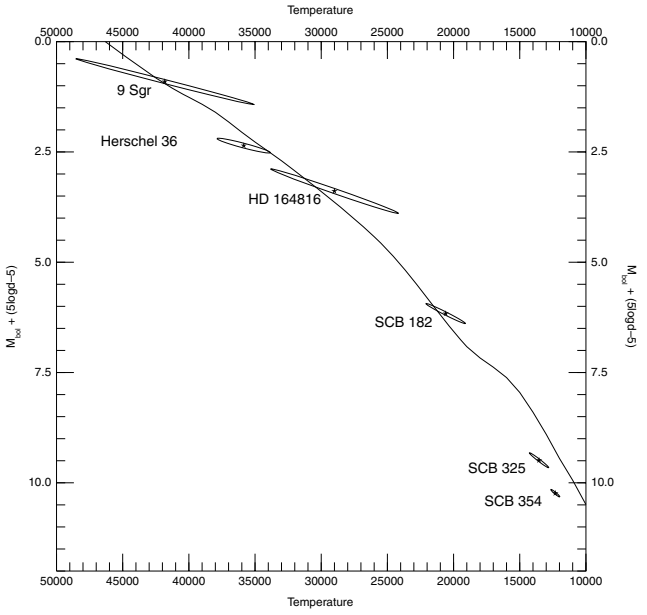

Figure 3. HR diagram compiled from the CHORIZOS output for the six stars in our sample. Ellipses indicate the 68 per cent likelihood contour for each star. The line shows the main sequence for $5 \log d - 5 = 10.5$. As seen in the plot, such a distance is compatible with the CHORIZOS output for the four earliest stars but not for the latest two.

As pointed out by van den Ancker et al. (1997), the study of a very young open cluster such as NGC 6530 cannot be performed using average extinction laws, because each star has its own individual extinction characteristics. In fact, anomalous extinction laws have been found for several stars embedded in the cluster. This may be a serious obstacle when deriving distance moduli from the observed optical colours, as done in most previous studies. In the infrared however, the greatly reduced extinction and the independence of the extinction law with the ratio of total to selective absorption R_V (Jones & Hyland 1980; Cardelli et al. 1989; Martin & Whittet 1990; Whittet et al. 1993) make distance determinations more reliable.

An alternative interpretation for the disagreement between the distance values derived by different authors may be that, when looking at the direction of NGC 6530, we are actually seeing distinct groups of stars placed at different depths. Fig. 10 in van den Ancker et al. (1997) shows the distribution of the distances of individual stars in the cluster, from which they estimated an average distance of 1.8 kpc. However, the distribution has a remarkable secondary peak around 1.5 kpc. In this way, the two B7-type stars analysed with CHORIZOS (SCB 325 and SCB 354) lead to distance moduli of 11.04 and 11.55, respectively. Both stars are located to the east of the Hourglass nebula, in a region with lower reddening, as inferred from their colour excesses $E(4405–5495) \sim 0.26$. So they presumably locate deeper in the spiral arm but are being observed through a window relatively free of dust. Finally, as mentioned above, Sung et al. (2000) also obtained two values for the distance modulus, but they left out the shorter distance estimate with the argument that many of the B-type stars were probably binaries.

Distance estimations to such very young open clusters are extremely complicated because they require knowledge of the extinction, which is really a result of circumstellar rather than intracluster material (van den Ancker et al. 1997). Each star has its own extinction law, and hence a very detailed study is needed. We conclude that a definitive distance to the Hourglass nebula is not yet established, but the CHORIZOS analysis of the earliest stars in the region is in favour of a distance modulus of 10.5 (1.25 kpc).

3.2 Photometry of infrared sources

Point spread function (PSF) photometry was performed using IRAF/DAOPHOT-II software running on a LINUX workstation. Stellar-like sources with fluxes significantly above the mean background were extracted using a threshold flux of 3σ. A set of PSF star candidates was selected in each image, avoiding nebular and crowded regions. The PSF was calculated using a Lorentz function and one look-up table. The final PSF photometry was performed on all the extracted sources using an aperture three pixels in radius. This corresponds to an aperture diameter which is roughly that of the measured full width at half-power of a typical stellar image.

Aperture corrections were computed between apertures of three and 15 pixels in radius using the same PSF stars. The final number of detected sources was 762 in K_s, 748 in H and 653 in J with sensitivity limits of 17.5, 18.5 and 19.2, respectively. The photometric limits were assumed to be the magnitude corresponding to the peak of the star distribution. This maximum occurred at about 1.5 mag brighter than the magnitude where the distribution fell to zero, i.e. 16.0 in K_s, 17.0 in H and 17.7 in J. The average photometric errors in all colours are 0.03 for sources with magnitude brighter than these limits and up to 0.2 for the faintest sources. Table 4 gives the position and photometry of all the infrared sources detected in the field. Running number sources are in column 1, columns 2 and 3 are right ascension and declination (J2000), columns 4–9 are J, H, K_s magnitudes and their errors, columns 10 and 11 are J–H and H–K_s colours, and column 12 contains comments related to the identification of optical counterparts.

In order to detect systematic photometric errors produced by aperture corrections and standard zero-points, we compared the magnitudes derived from our photometry for some relatively bright stars with those from the 2MASS PSC (Second Incremental Data Release; Cutri et al. 2000). Considering only the sources in the 2MASS with photometric quality '*AAA*', we found an average difference in J, H and K_s magnitudes of 0.005 ± 0.085, 0.016 ± 0.052 and 0.008 ± 0.067, respectively, so no further correction was performed.

Positions in equatorial coordinates for the individual sources were established based on the 2MASS PSC (All-Sky 2003). The rms residuals between the positional tables from this work and from the 2MASS data base are found to be 0.11 and 0.12 arcsec, in α and δ, respectively.

3.3 Colour–colour and colour–magnitude diagrams

A near-infrared CC diagram of the Hourglass region is illustrated in Fig. 4 for the 647 sources in the field detected in all three wavelength bands. Also plotted in Fig. 4 is the locus of points corresponding to the position of the unreddened main sequence and the position of the red giants. The two parallel dashed lines represent the reddening vectors for early-type (O3 V) and late-type (M0 III) stars, determined using the values of extinction from Rieke & Lebofsky (1985); their length corresponds to $A_V = 20$ mag. Fig. 5 shows the K_s, $(H-K_s)$ CM diagram for the same stars. The position of the main sequence has been plotted, corrected to an apparent

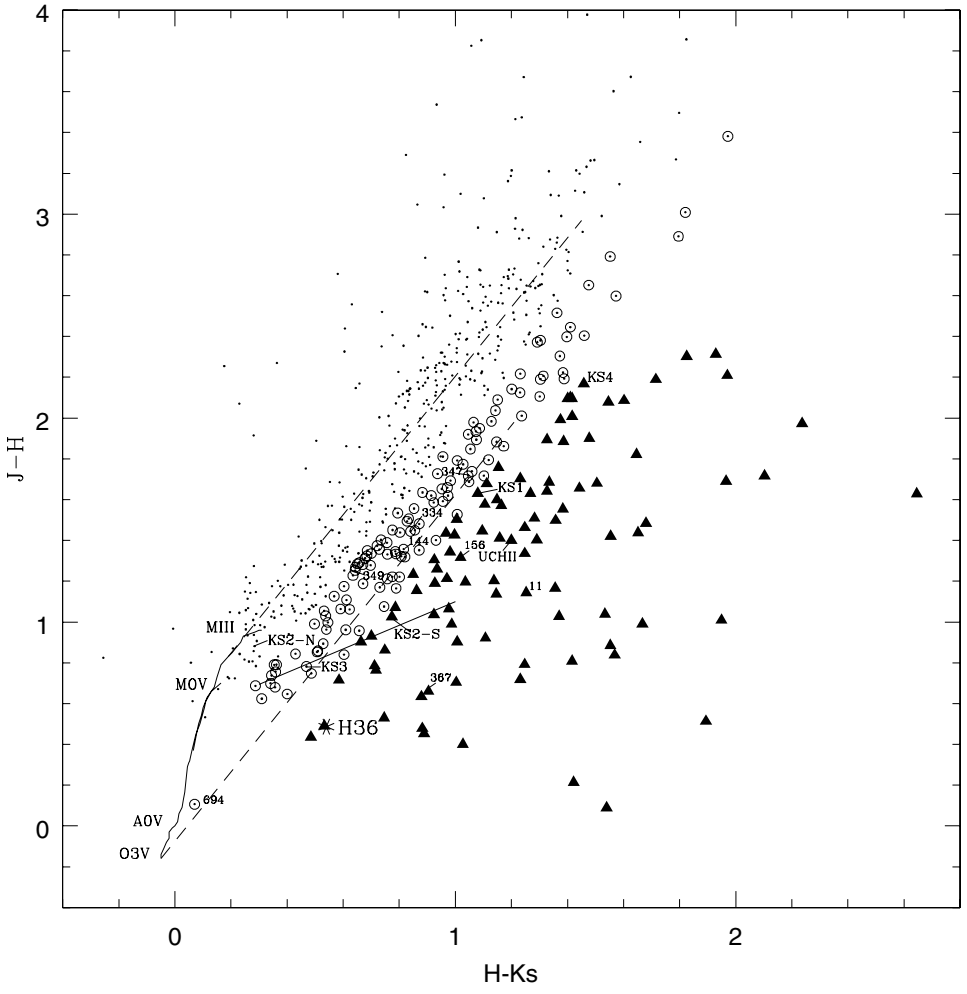

Figure 4. Near-infrared CC diagram for the Hourglass region. The continuous line marks the locus of main-sequence and giant stars. The two parallel dashed lines represent the reddening vectors for a visual extinction of $A_V = 20$ mag. The loci of classical T Tauri stars (CTTS) from Meyer et al. (1997) is also shown as a straight line from $H-K_s = 0.3$ to $H-K_s = 1.0$. Sources with evident infrared excesses are plotted with filled triangles. Open circles denote either CTTS with moderate to large reddening or extremely reddened early-type main-sequence dwarfs. Sources marked with points are expected to be foreground/background field objects. Some interesting infrared sources (see text) are labelled.

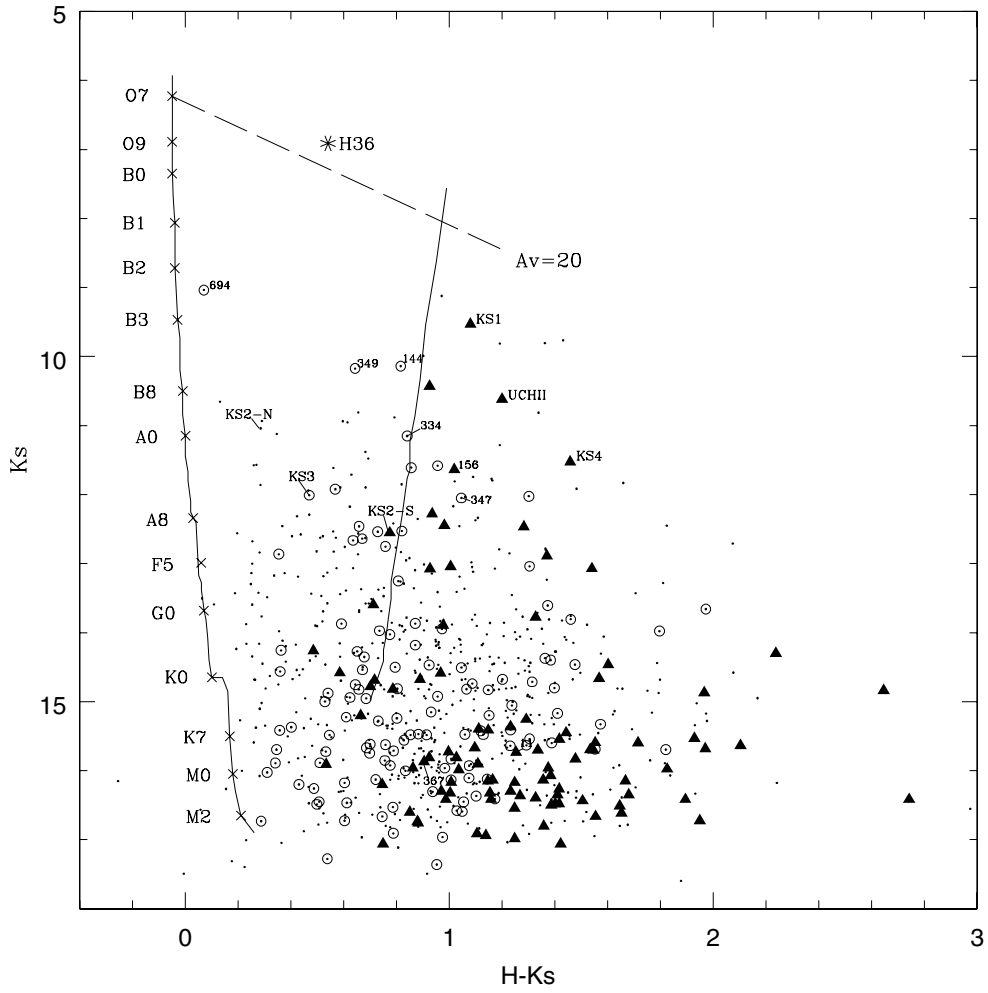

Figure 5. Near-infrared CM diagram for the Hourglass region. The location of the main sequence is shown using a distance modulus of 10.5 mag. The red giants are represented by a vertical solid line, shifted to the distance of the Galactic bulge (8 kpc) and reddened by $E(H{-}K_s) = 0.64$ because of the interstellar component. The dashed line represents the standard reddening vector with length $A_V = 20$ mag. Symbols and object labels are the same as in Fig. 4.

distance modulus of 10.5, which, as was previously discussed, is appropriated for the Hourglass region. The reddening vector for an O7 V is also plotted for a visual extinction of 20 mag. The vertical solid line denotes the location of giant stars (Koornneef 1983; Zombeck 1990) for the distance of the Galactic bulge (8 kpc) and reddened by $E(H{-}K_s) = 0.64$ as a result of the interstellar component. The position of Her 36, using near-infrared data from the 2MASS, has been marked for reference. We note here that, if we compare the data with the zero-age main sequence (ZAMS) instead of the main sequence, both Her 36 and SCB 182 (source 694) fall about 1 mag above the expected location according to their spectral types (O7.5 V and B2.5 V, respectively). This shift is even larger ($\sim$2 mag) considering the distance modulus of 11.3 suggested by other authors.

As M8 is located not far from the direction to the Galactic Centre, many field interlopers can be expected. In particular, it is very probably intercepting part of the giant population of the galactic inner disc and bulge. In this way, the CC and CM diagrams show a superposition of well-distinguished stellar components. Unfortunately, no control fields were taken for these observations, but in order to account for the distribution of the foreground/background field stars, JHK_s photometry corresponding to a 5-arcmin radius circular field located off the nebula at $\alpha(2000) = 270.654$ and $\delta(2000) = -24.618$ ($\sim$18 arcmin in l at the same b) was retrieved from the 2MASS catalogue. We considered only the sources with photometric errors lower than 0.1 mag. This field was chosen to be free of significant interstellar material by examination of *IRAS* surveys in the region. Based on these data we studied the $(H{-}K_s)$ distribution of the field stars, which shows a significant concentration of sources around $(H{-}K_s) = 0.8$, probably indicating the average colour of the bulge red giants, which must be highly affected by interstellar reddening (see Fig. 6). A similar analysis for the sources with $K_s < 14$ of the Hourglass field revealed a peak around $(H{-}K_s) = 1.0$, with a considerable spread to larger values, because of the differential extinction originated in the molecular cloud. In addition, both histograms show a secondary peak around $(H{-}K_s) = 0.3$, probably associated with main-sequence stars moderately affected by reddening. We note here that the number of infrared sources detected in the Hourglass field almost doubles the number expected from the ratio of the areas of the on and off field observations. Two facts can account for this: the existence of an infrared cluster around Her 36 and the much higher resolution of our observations.

Using 2MASS data we also constructed the CC and CM diagrams for the control field (Fig. 7). The CC diagrams for the control field and the Hourglass region clearly differ. The stars in the control field

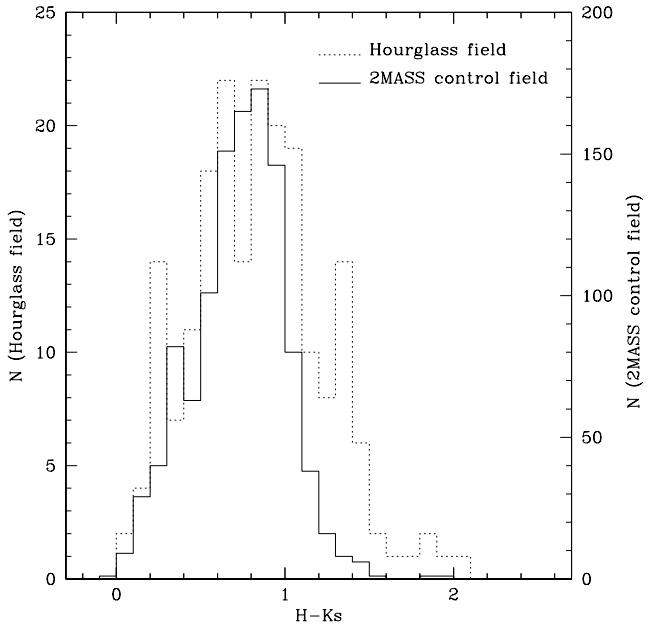

Figure 6. Distribution of $(H–K_s)$ colours for the Hourglass field (dashed line) and the 2MASS control field (solid line). The peak around $(H–K_s) = 1.4$ observed in the Hourglass field can be account by the near-infrared excess sources associated with the cloud.

appear confined in two regions: a very crowded region corresponding to the highly reddened giants of the bulge and disc, and a less populated region associated with field main-sequence stars with little reddening. However, the stars in the Hourglass region spread over a much larger area of the CC diagram. Besides the two components observed in the control field, which confirm that a significant fraction of the stars are background field stars unrelated to the cloud, there are a significant number of sources located along and to the right of the reddening vector of an O dwarf star. These stars with intrinsic colours indicative of near-infrared excess emission must be associated with young stellar objects (YSOs), such as Class I 'protostars', Herbig Ae/Be objects and T Tauri stars.

In Fig. 4 two types of symbols have been used to discriminate between objects of different nature. In this way, filled triangles represent sources with evident infrared excess, which are prime candidates to be included among the YSOs previously mentioned. Open circles may denote either classical T Tauri stars affected by moderate to large amounts of reddening, or extremely reddened early-type main-sequence stars. For example, according to its position in the CC and CM diagrams, source 349 could be either a classical T Tauri star with $A_V \sim 4$ mag, or an early B-type star affected by more than 11 mag of extinction. Spectroscopic observations are needed for a definitive conclusion.

Also evident from Fig. 4 is the lack of stars within the lower part of the reddening band $[0 < (H–K_s) < 0.3]$, reflecting a threshold in the extinction caused by the presence of the molecular cloud. Just beside this gap, there is a group of sources vertically distributed around $(H–K_s) = 0.3$, which presumably represents the main sequence at the Hourglass distance. This idea is supported by the presence of a similar distribution $(H–K_s) = 0.3$ to the right and parallel to the main sequence of the CM diagram. If so, the mean extinction toward the region can be estimated from a simple approximation (Rieke & Lebofsky 1985), $A_K = 1.78 \times E(H–K)$, adopting for the main-sequence stars an average intrinsic colour excess of 0.2 mag. This leads to $A_K = 0.36$ mag ($A_V = A_K/0.112 = 3.2$ mag).

The CM diagrams for the control and the Hourglass fields are also clearly different. The bulk of the stars in the control field distribute in a band around $(H–K_s) = 0.8$ (which approximately coincides with the vertical line that represents the location of red giants for the distance of the Galactic bulge), in contrast with the Hourglass field, where the sources appear in a wider range of $(H–K_s)$ and a great number of them show large values of this colour. The large $(H–K)$ colour for these sources is likely intrinsic and a result of excess infrared emission, as deduced from their locations in the infrared excess region of the CC diagram.

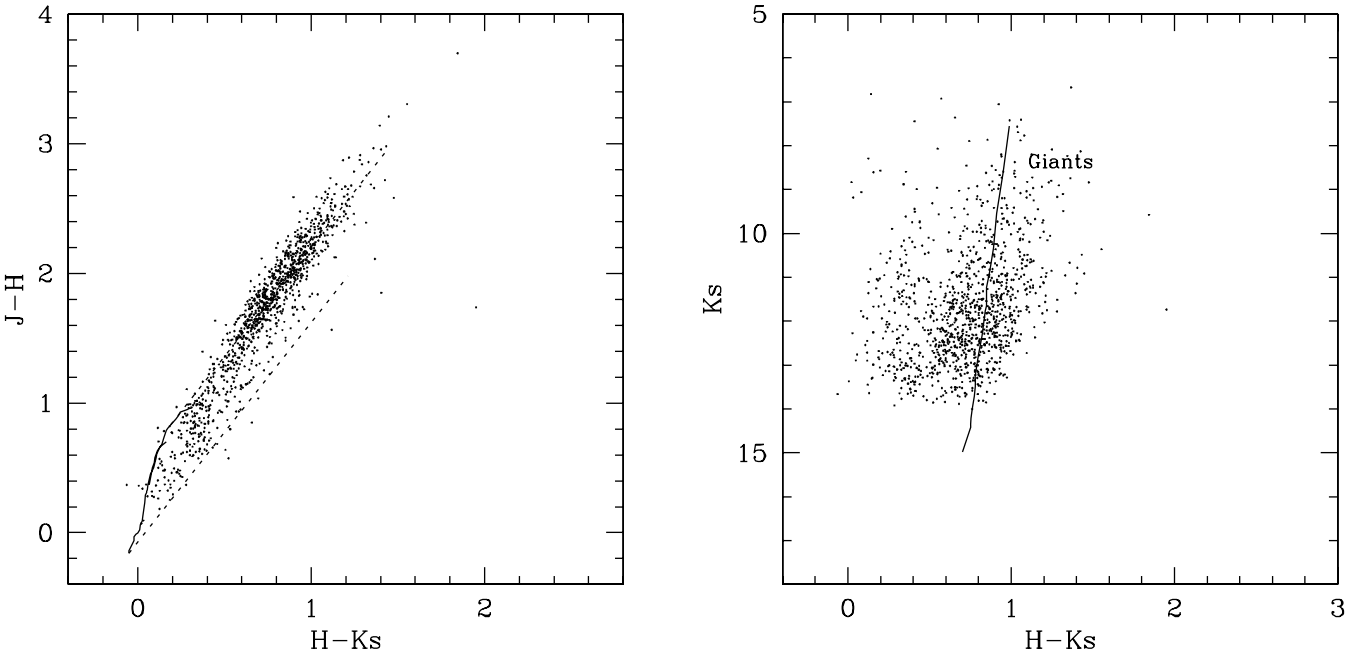

Figure 7. Near-infrared CC and CM diagrams for the 2MASS control field. The solid line represent the location of giants for the distance of the Galactic bulge (8 kpc) and reddened by $E(H–K_s) = 0.64$ mag because of the interstellar component.

Before concluding this section, we want to stress that the comparison of the infrared photometric diagrams suggests that an important fraction of the stars observed toward the Hourglass nebula are background field stars unrelated to the cloud, presumably red giants of the galactic inner disc and bulge. These objects are significantly reddened as a result of interstellar extinction through the line of sight, plus a differential contribution of an inhomogeneous molecular cloud, which, as will be discussed in next section, possesses clumps dense enough to block background radiation.

As previously mentioned, when we observe in the direction of M8 we are actually seeing a superposition of distinct stellar populations placed at different distances from us, which significantly complicates the interpretation of the results. Trying to clarify this situation, we divided the infrared sources observed toward the Hourglass in six groups according to their infrared colours. Groups I, II, III and IV include sources located above the track [$J–H = 1.7 * (H–K_s) + 0.2$], with $H–K_s < 0.4$, $0.4 < H–K_s < 0.8$, $0.8 < H–K_s < 1.2$ and $H–K_s > 1.2$, respectively. This track has been chosen as the straight line parallel to the reddening vectors, passing approximately through the blue end of the classical T Tauri loci of Meyer, Calvet & Hillenbrand (1997). In some way it may be considered as a dividing line between early- and late-type stars, as it coincides with the reddening track of a mid-F-type dwarf. Because these sources are expected to be members of the stellar population of the inner disc and bulge, we call them 'giants', even though group I may have a contribution of late-type main-sequence dwarfs with lower reddening. Groups V and VI include sources below the former track. Whereas group V is expected to contain both classical T Tauri stars with lower reddening and/or highly reddened early-type dwarfs, group VI will include only objects with genuine infrared excess. In Fig. 8 we have plotted the spatial distribution of each stellar group using different symbols and colours. A colour CC diagram has been included for reference.

Furthermore, in order to quantify the complex distribution of sources in the region, we subdivided the observed field in nine areas of about 45 × 45 arcsec^2, which we call from upper left to lower right, NE, N, NW, E, C, W, SE, S and SW, respectively, and we counted the number of stars of each group in every subregion. The resulting star counts are presented in Table 2. The interpretation of Fig. 8 and Table 2 will be discussed in the following subsections.

3.4 Extinction map

We note here that, in contrast to other studies of dust extinction in molecular clouds (e.g. Lada et al. 1994), it is not easy to infer the mean intrinsic colour ($H–K$) of background stars from the control field stars, because these objects themselves suffer significant random extinction because of a large depth in the line of sight. Anyway, we choose ($H–K$) = 0.15 as a representative value, which is equivalent to the colour of an early K star, and follow the procedure described in Lada et al. (1994), in order to map the distribution of colour excesses (and hence extinctions) through the cloud. We derived the mean colour excess for all the sources located along the reddening vector of a giant star in the Hourglass CC diagram, i.e. all the candidate late-type stars of the galactic inner disc and bulge. In a rough approximation, these can be considered as the objects in the groups I, II, III and IV introduced in Section 3.3. These measurements were then converted to a mean extinction in the K band, A_K, using the reddening law from Rieke & Lebofsky (1985):

$$A_K = 1.78\, E(H–K).$$

We consider A_K instead of the visual extinction $A_V = 15.9\, E(H–K)$, because the latter expression is valid only to the extent that the reddening law in this cloud is a normal one. Disregarding the objects in groups V and VI (plotted with magenta and red, respectively), which can be roughly adopted as belonging to the M8 region itself, Fig. 8 (bottom) represents a randomly sampled map of the distribution of extinctions across the Hourglass nebula, obtained by plotting the position of each field star with a circle whose size and colour depend on the total extinction derived from its infrared colours (from

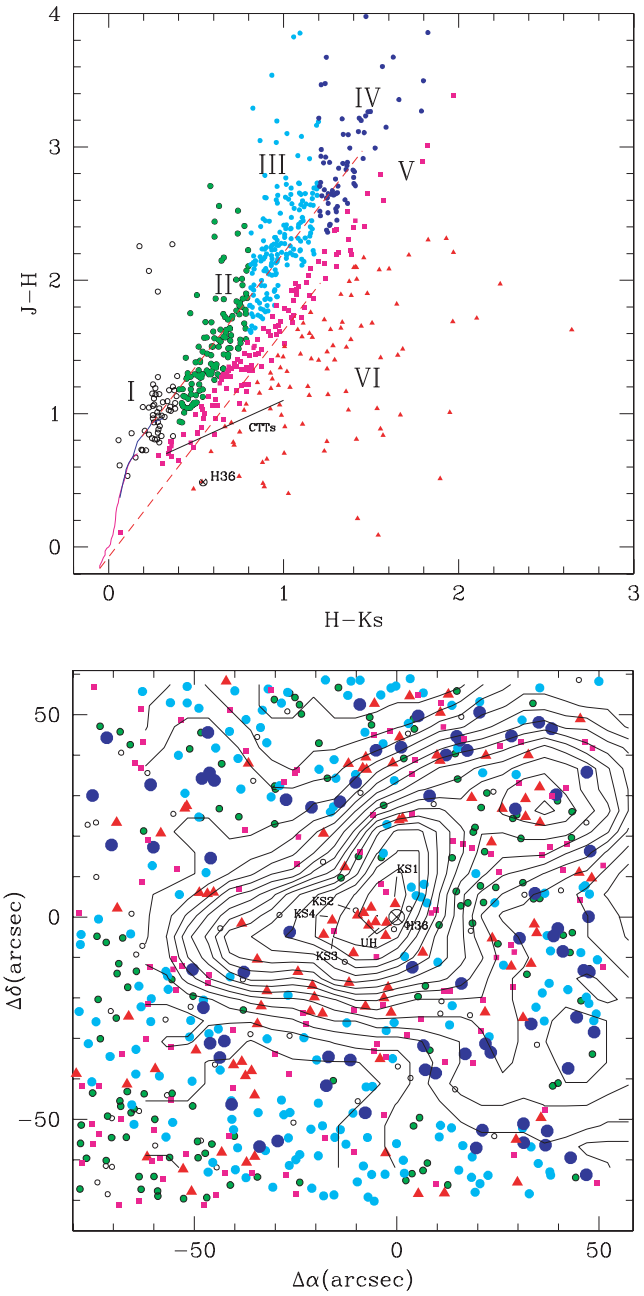

Figure 8. Upper panel: CC diagram for all the sources in the Hourglass nebula. Open, green, cyan and blue circles denote sources in groups I, II, III and IV, respectively (referred to as 'giants' in the text). Magenta squares represent the sources in group V, and red triangles the genuine infrared excess objects of group VI. Lower panel: spatial distribution of the different stellar groups observed towards the Hourglass nebula. The positions of Her 36, the infrared sources KS 1 to KS 4 and the ultracompact H II region G5.97–1.17 are marked. CO $J = 3$–2 contours from White et al. (1997) are also shown for comparison. Symbols are the same as in the previous panel.

Table 2. Star counts of different stellar populations in the Hourglass region.

	Subregion									
Group	NE	N	NW	E	C	W	SE	S	SW	Sum
I	6	5	5	9	7	6	12	5	3	58
II	10	17	15	12	5	19	33	9	7	127
III	14	29	8	20	9	23	22	38	17	180
IV	9	8	13	4	2	11	4	8	14	73
V (ms)	10	13	15	12	10	16	25	11	7	119
VI (ex)	6	11	14	6	27	9	13	5	4	95
Sum	55	83	70	63	60	84	109	76	52	652
'Giants' (I+II+III+IV)	39	59	41	45	23	59	71	60	41	438
ms+ex (V+VI)	16	24	29	18	37	25	38	16	11	214
Ratio ex/giants	0.15	0.19	0.34	0.13	1.17	0.15	0.18	0.08	0.10	0.22
Ratio (ms+ex)/giants	0.41	0.41	0.71	0.40	1.61	0.42	0.54	0.27	0.27	0.49
Ratio ex/ms	0.60	0.85	0.93	0.50	2.70	0.56	0.52	0.45	0.57	0.80

the largest to the smallest extinction, we have big blue, cyan, green and open circles). In spite of the depth of our infrared observations, the centre of the cloud remains devoid of stars, indicating the presence of extremely high extinctions. Also evident is the existence of an extinction gradient extending from the position of Her 36. In Fig. 8 we overlay a contour map of the integrated CO $J = 3$–2 emission from White et al. (1997). The correspondence between our extinction map and the distribution of molecular material is impressive, demonstrating that the extinctions derived for the individual candidates for background giants are good tracers of the molecular cloud.

3.5 Infrared cluster around Herschel 36

Using photometry, 763 sources have been extracted from a 135 × 139 arcsec^2 area around the massive star Her 36, the vast majority of which had not been detected by previous observations. 652 of these sources have been detected in all three wavelength bands and are plotted in the CC and CM diagrams in Figs 4, 5 and 8. The analysis of these infrared diagrams leads us to suggest that an important fraction of the stars observed toward the Hourglass are background field stars, probably red giants of the inner disc and bulge. Adjusting for this background contamination is however extremely difficult. Although somewhat rough, a direct alternative is to consider the extreme case in which all the sources in groups I, II, III and IV are foreground/background field stars, while all the sources in groups V and VI belong to the cluster (see Section 3.3 and Fig. 8 for the definition of the stellar groups). Then the number of infrared sources expected to be related to the region may be about 214. 95 of these show genuine moderate and large infrared excesses, yielding a fraction of near-infrared excess sources of about 45 per cent. We should keep in mind that we have presumably overestimated the number of objects associated with the molecular cloud, and therefore the resulting fraction of infrared excess sources may be only a lower limit. Anyway, the estimated value is close to the fraction found within the Taurus (50 per cent; Kenyon & Hartmann 1995), NGC 1333 (60 per cent; Lada, Alves & Lada 1996) and S87E (40 per cent; Chen et al. 2003) star-forming regions. A strikingly important fact is what happens in the central part of the field (subregion C in Table 2), where the infrared excess objects reach a total of 27 or over 70 per cent of all the point sources assumed to belong to the cluster. From the analysis of molecular hydrogen and CO emission, Burton (2002) suggested the existence of a molecular outflow from Her 36. This fact, along with the relative large fraction of infrared excess sources and the morphological evidence of jets from some of them (see Section 3.8), indicates the cluster population is extremely young. From the comparison with similar star-forming regions for which ages have been estimated (see section 5 in Lada et al. 1996), we could say that this cluster is probably between 1 and 2 × 10^6 yr, if not younger.

CO line emission toward the Hourglass nebula was studied by White et al. (1997), who detected an elongated molecular core, 30 × 20 arcsec^2 in size and orientated SE–NW. The superposition of CO $J = 3$–2 contours on the spatial distribution of sources in the field is shown in Fig. 8. The CO emission peaks at Her 36 and 40 arcsec to the north-west. Note that the first peak is the second most intense CO source observed with a single dish antenna.

As clearly seen in Fig. 8, the infrared excess sources do not distribute uniformly in the region. Instead, they extend along the molecular core. While Her 36 and the infrared sources KS 1 to KS 4 designated by Woodward et al. (1990) lie close to the most intense peak, another group of candidate YSOs coincides with the secondary peak. Additionally, a number of sources with infrared excess appear grouped to the south of the Hourglass, within the cavity open by the strong wind of Her 36. It is remarkable that almost no source is detected to the north-east of Her 36, either with or without infrared excess, indicating an extremely high density of the molecular cloud.

The infrared excess sources distribution can be quantitatively described using the star counts in Table 2. Three representative ratios between distinct stellar populations have been computed. The ratio of genuine infrared excess sources to candidate late-type objects, ex/'giants', has a very low value (∼0.15 on average) in seven of the nine regions in which the Hourglass field was subdivided (see Section 3.3). Nevertheless, it greatly exceeds its average value in the north-west region and reaches 1.17 in the central (C) region. These two areas approximately coincide with the secondary and primary CO emission peaks respectively, confirming that the youngest objects locate along the molecular core.

3.6 Individual stars

Among the most peculiar objects in the field we find the infrared sources designated by Woodward et al. (1990) as KS 1 to KS 4, as

well as the ultracompact H II region G5.97–1.17 studied by Stecklum et al. (1998). What follows is a brief description of the infrared properties of these objects.

(i) KS 1. This source (312) is ∼3.3 arcsec north and ∼0.3 arcsec east of Her 36. Allen (1986) suggested that this star and Her 36 may be part of a Trapezium-like stellar cluster, based on the similar separation distances. KS 1 is actually a binary star with a very red northern component, as pointed out first by Stecklum et al. (1995). The binarity of this object compelled us to perform aperture photometry on it. According to its near-infrared colours ($K_s = 9.53$, $J–H = 1.63$, $H–K_s = 1.08$), it is very probably a Herbig Ae/Be object affected by a few magnitudes of visual extinction.

(ii) KS 2. Located ∼1.5 arcsec north and ∼11.1 arcsec east of Her 36, this star is also a binary system. In our PSF photometry we identified two well-separated (angular separation ∼1.3 arcsec) sources: 385 (north) and 382 (south). While source 385 (KS 2-N) is presumably a late B-type dwarf attenuated by ∼5 mag of visual extinction, the infrared colours of source 382 (KS 2-S) are typical of a classical T Tauri star ($K_s = 12.55$, $J–H = 1.03$, $H–K_s = 0.77$).

(iii) KS 3 and KS 4. These two sources are located ∼16.8 arcsec east of Her 36, very near the apex of the optical bicone (the 'waist') of the Hourglass. The observed infrared colours of KS 3 (410) can be replicated either by a relatively hot ∼ B9/A0 dwarf affected by ∼8 mag of visual extinction, or by a cooler T Tauri star ($K_s = 12.01$, $J–H = 0.78$, $H–K_s = 0.47$). However, KS 4 (414) is much redder than KS 3 and shows significant near-infrared excess emission. Its position on the CC diagram is typical of very young stellar objects such as Class I protostars ($K_s = 11.53$, $J–H = 2.17$, $H–K_s = 1.46$).

(iv) UC H II region G5.97–1.17. High-resolution optical, infrared and radio observations revealed that this object, 2.7 arcsec distant from Her 36, may be a proplyd, i.e. a young star surrounded by a circumstellar disc that is being photoevaporated by the nearby hot star (Stecklum et al. 1998). Because of its close proximity to Her 36, we had to perform aperture photometry on this source (330). The near-infrared colours obtained indicate that G5.97–1.17 likely belongs to the class of Herbig Ae/Be objects ($K_s = 10.62$, $J–H = 1.40$, $H–K_s = 1.20$).

3.7 Distribution of dust and gas

Using *HST* images, we have produced maps of the following line ratios: Hα/Hβ (Balmer ratio) and ([S II]6717+[S II]6731)/Hα (S2H ratio). Fig. 9 shows the Balmer ratio map. The Hα map has been included in Fig. 10 for reference. The Balmer ratio can be used as a tracer of extinction by dust. For temperatures of $\sim 10^4$ K and electron densities of ∼100 cm^{-3}, the theoretical Hα/Hβ value is 2.86 (Osterbrock 1989). The presence of extinction increases the observed ratio, because it affects Hβ wavelengths more than Hα wavelengths. The measured ratio will depend on the geometry of the dust and gas clouds, as well as on the extinction law.

As seen in Fig. 9, the Balmer ratio goes clearly above the expected value of 2.86 over the whole region of the Hourglass. In fact, it has a minimum value close to 4.0. We interpret this effect as a consequence of the interstellar extinction toward the Hourglass nebula. A colour excess $E(B–V)$ can be associated with a measured ratio $r_B = I(\mathrm{H}\alpha)/I(\mathrm{H}\beta)$ according to the expression

$$E(B–V) = E_0 \log_{10}(r_B/2.86),$$

where E_0 is a constant which depends on the reddening law. If we adopt the extinction law parametrized by Cardelli et al. (1989), $E_0 = 2.307$, and then $E(B–V) = 0.34$ when $r_B = 4.0$. This is in excellent agreement with the mean value of the reddening derived from the optical colours of the stars in NGC 6530 [$\langle E(B–V)\rangle = 0.35$; Sung et al. 2000].

The distribution of dust in the central part of the nebula is quite complex, showing strong variations in an arcsec scale, which is clearly appreciable in the enlargement shown in the upper-right corner of the panel. The whole central area seems to be highly reddened and the maximum values of r_B are found around Her 36 [$r_B > 7$ and $E(B–V) > 0.9$]. The region immediately to the east of Her 36 shows an interesting spatial correlation between r_B (Fig. 9) and Hα (Fig. 10): brighter (in Hα) regions present higher values of r_B, rather than the opposite, which is what would be expected if optically thin clouds were partially occulting the ionized gas behind. Furthermore, the correlation is also apparent when comparing the spatial distribution of Hα and the S2H ratio in the sense that low values of the S2H ratio correspond to bright areas. Similar correlations have been detected in NGC 604 (Maíz-Apellániz, Pérez & Mas-HessePérez 2004) and in 30 Doradus (Walborn et al. 2002; Maíz Apellániz et al. in preparation) and can be explained if the variations in extinction are caused by optically thick clouds instead of by optically thin clouds. In such a model, a strong variable foreground screen is present and located between the main part of the H II region and the observer. In those areas where the screen is thinner, we can see into the bright part of the H II region but at the cost of measuring large values of r_B (note that values of r_B larger than about 4.0 imply that dust and gas cannot be uniformly mixed but rather that the dust is located in a foreground screen; Maíz-Apellániz et al. 2004). There, the gas we are seeing is directly exposed to the ionizing radiation of Her 36, located a short distance away, and therefore shows a high excitation, implying low values of the S2H ratio. In those areas where the screen is thicker, dust completely blocks the bright areas of the H II region and all we can see is the back side (as seen from Her 36) of the cloud, which only receives low-intensity ionizing radiation (scattered from Her 36 or originating from other ionizing sources at large distances; see fig. 8 of Maíz-Apellániz 2006), thus producing H II gas with a low ionization parameter. There, the S2H ratio is much higher, as expected, and r_B is lower because there is little dust between the source and the observer because the cloud is located at larger distances than the source.

Extinction seems to be fairly uniform over the rest of the field. The cavity toward the south open by the winds of Her 36 (marked with a letter C in Fig. 9) suffers almost no obscuration, thus showing the lowest values of r_B, i.e. $4.0 < r_B < 4.5$, or equivalently, $0.34 < E(B–V) < 0.45$. A kind of thin flap of dust seems to cover all the region toward the west of Her 36. This fact implies that we are not actually penetrating the molecular cloud but only detecting the front gas Hα emission, which can explain the relatively low extinction measured [$r_B < 5$ and $E(B–V) < 0.56$].

By comparing the Balmer ratio and the Hα emission, we find a number of dark regions with very low Hα intensity [$I(\mathrm{H}\alpha) < 0.5$] which also show small values of r_B ($r_B \sim 4.0$). An example of such region has been marked with a letter A in Fig. 9. Here, a low r_B does not mean low extinction. On the contrary, the optical depth is so high that in the case of existing gas emission hidden by dust, it cannot be detected only with optical data. Such possible emitting regions should be unveiled using near-infrared Brγ imaging.

To conclude, we want to stress that extinctions derived from the Balmer emission lines are only representative of the outer 'shell' of the nebula, up to about $A_V \sim 3$ mag. Optical observations do not probe the gas and dust distribution more deeply into the cloud, and thus estimating ionizing fluxes and other properties only from

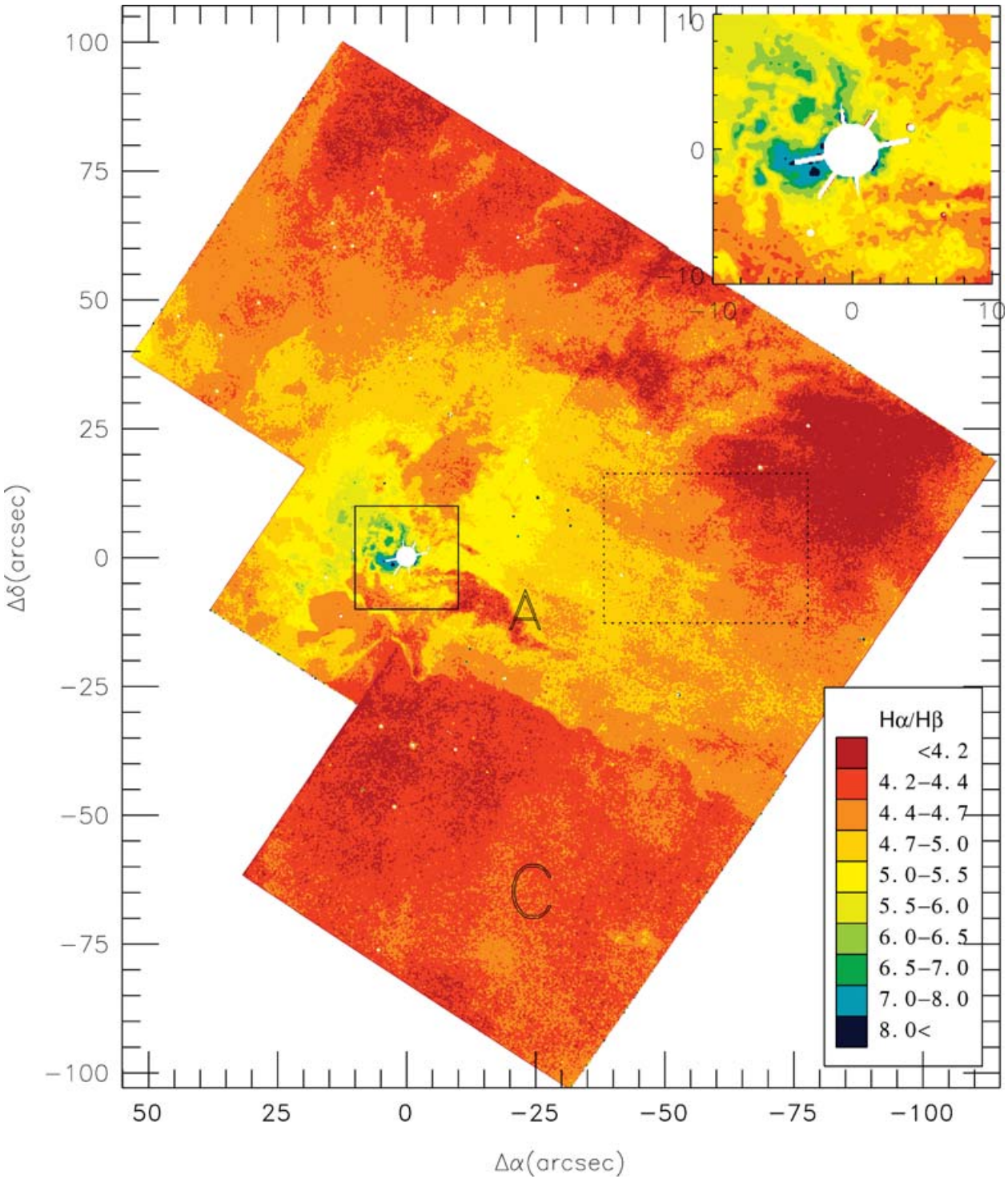

Figure 9. Balmer ratio map of the Hourglass region. An enlargement of the central part is shown in the upper-right corner of the panel. The letters A and C refer to the regions described in the text (see Sections 3.7 and 3.8). The dashed-lined rectangular box defines the region shown in Fig. 15.

optical data will lead to uncertain results. Near-infrared imaging is inevitably needed to analyse what processes are really taking place behind the dust.

3.8 Signatures of ongoing star formation in *HST* images

Archival *HST* emission-line images in Hα, [O III] and [S II] were searched for proplyds, jets and other features that might be associated with the newly detected candidate YSOs. The *HST* observations reveal a rich variety of structures related to star formation, similar to those observed in M16 and M42.

Herbig–Haro (HH) objects are shock-excited nebulae powered from YSOs (see Reipurth & Bally 2001). The morphological analysis of [S II] images is a commonly used technique for surveying star-forming regions for the location of excited gas arising from

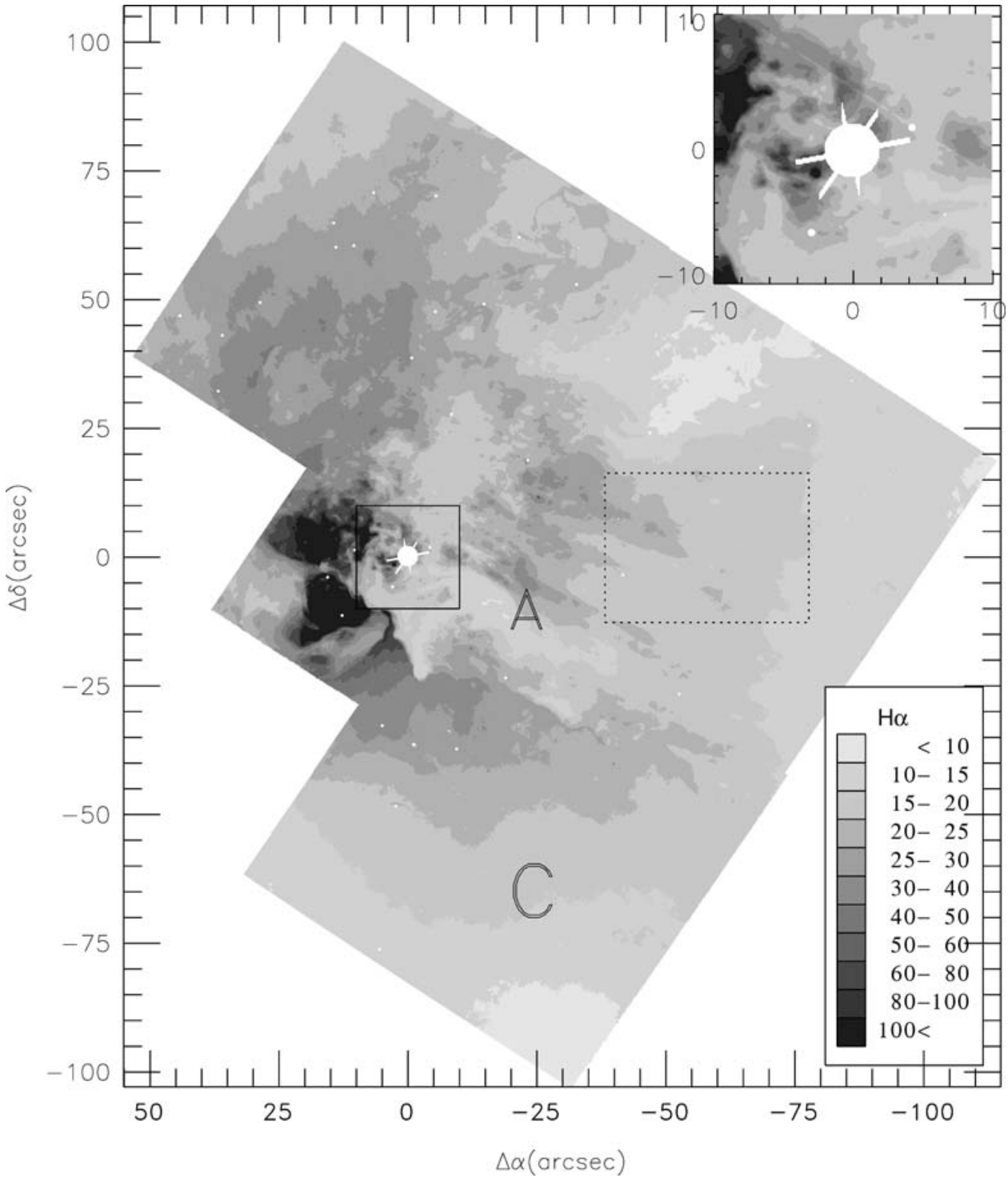

Figure 10. Hα map of the Hourglass region. An enlargement of the central part is shown in the upper-right corner of the panel. The letters A and C refer to the regions described in the text (see Sections 3.7 and 3.8). The dashed-lined rectangular box defines the region shown in Fig. 15. The surface brightness units are 10^{-16} erg cm^{-2} s^{-1} per WFC pixel.

HH flows (e.g. Wang et al. 2003). This is helped by the analysis of [S II]/Hα ratio maps in which regions with high values indicative of shock-excited gas are searched.

Figs 11 and 12 show the *HST* [S II] continuum-subtracted emission map and the corresponding [S II]/Hα (S2H) ratio map of the Hourglass nebula, respectively. The strongest line emission arises from the inner part of the Hourglass and is mainly concentrated on the east wall of the cavity. Both the [S II] and the Hα emissions have a clumpy structure close to Her 36. When compared to Hα emission, the [S II] emission shows a more complex and filamentary pattern to the north and west of the nebula. However, both images look smoothed in the southern part of the nebula, where the H II cavity

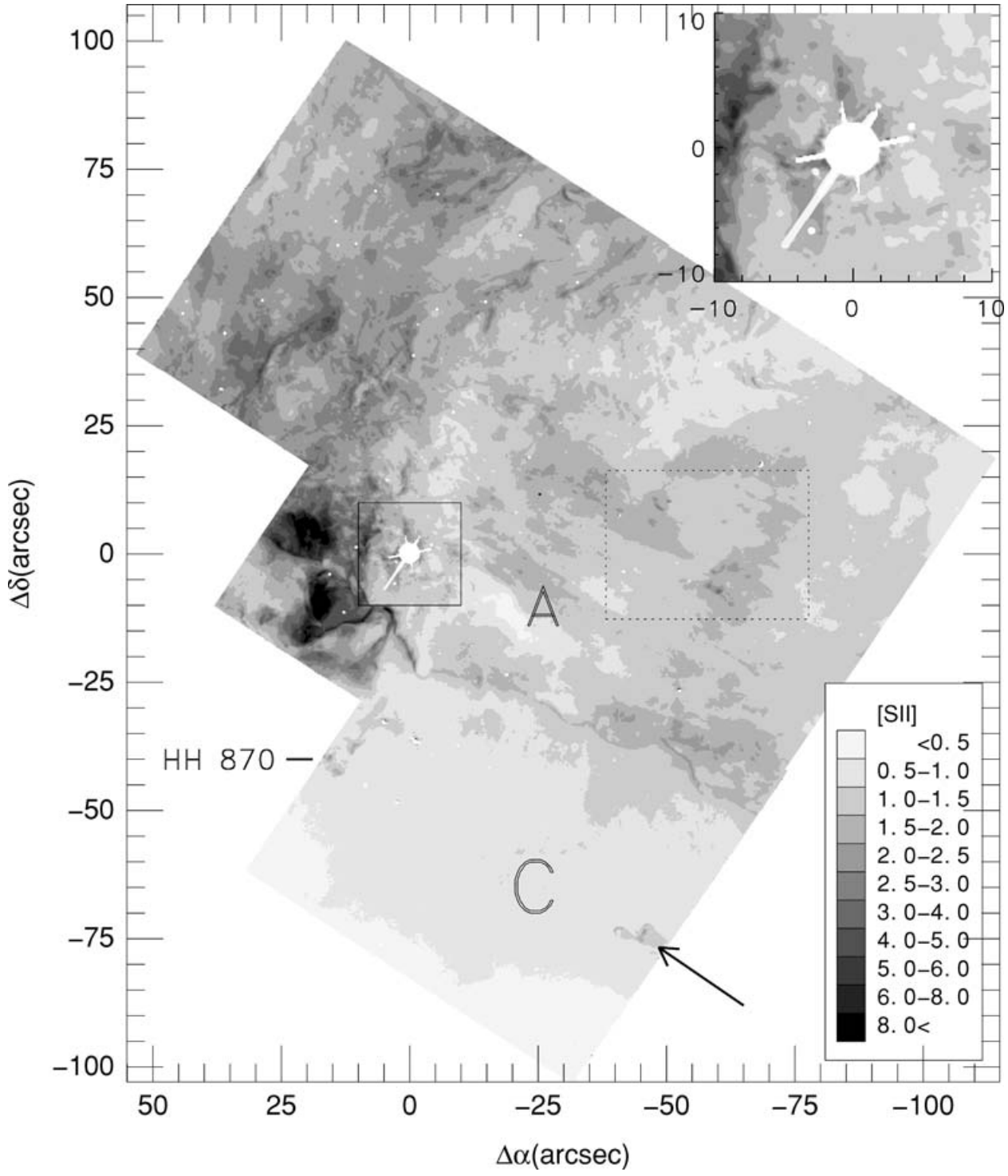

Figure 11. [S II] emission map of the Hourglass region. An enlargement of the central part is shown in the upper-right corner of the panel. The letters A, B and C refer to the regions described in the text (see Sections 3.7 and 3.8). The dashed-lined rectangular box defines the region shown in Fig. 15. The arrow indicates the direction to the O-type star 9 Sgr, located 4.12 arcmin from the finger-shaped molecular globule. The surface brightness units are 10^{-16} erg cm^{-2} s^{-1} per WFC pixel.

is an opened blister. These differences in the emission appear as large fluctuations in the S2H map, in a scale of few tenths of arcsec, especially close to Her 36 and to the west part of the image.

It is very interesting to note that the S2H flux ratio goes below 0.10 over almost the whole region of the Hourglass, as expected for a photoionized plasma. We are particularly interested in detecting emission features produced in shock-excited gas, for which the expected S2H flux ratio values are typically of 0.3–0.5. Nevertheless, the highest S2H flux ratio hardly reaches 0.2 (over an arc located at 75 arcsec to the north-west of Her 36). This could be

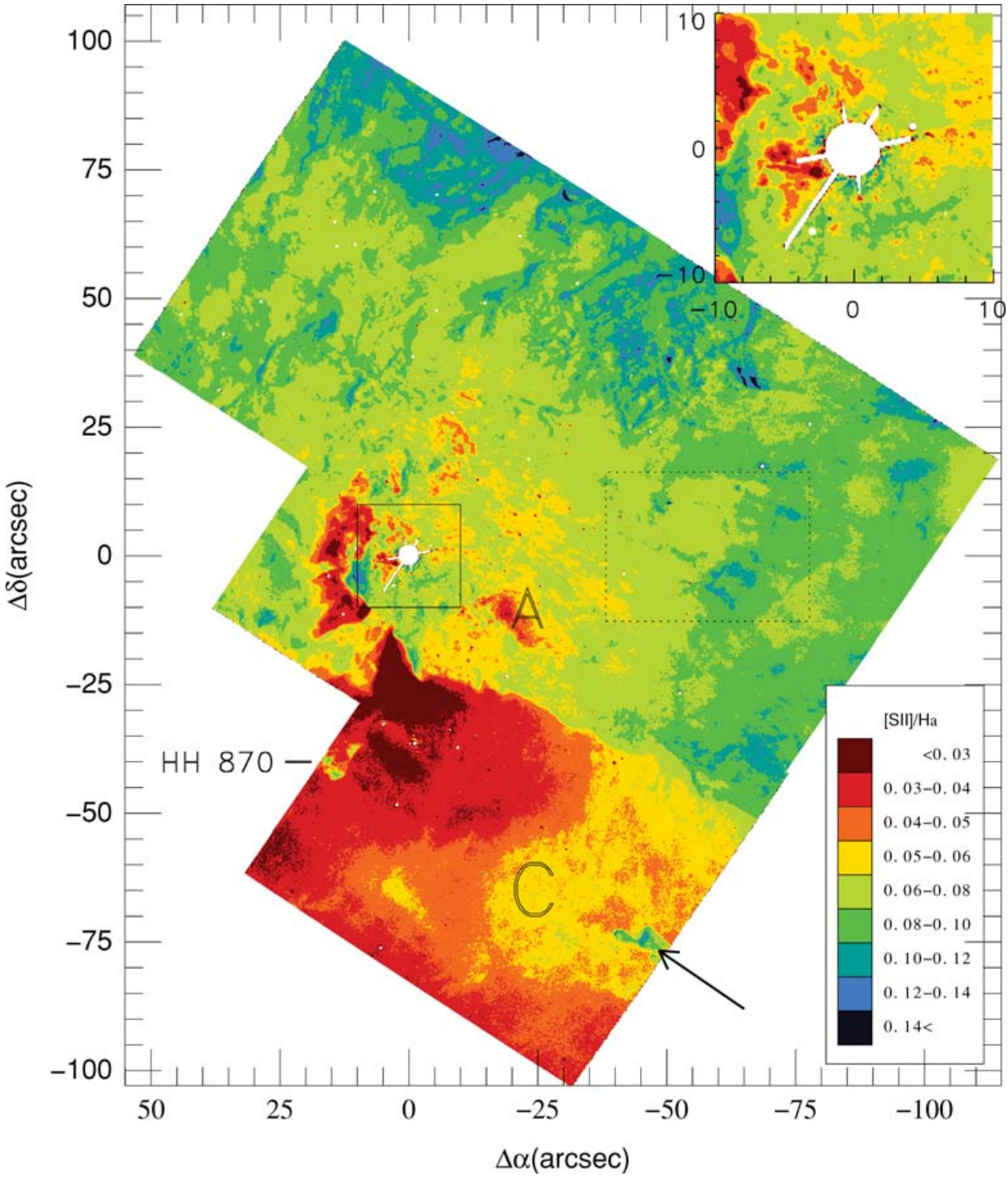

Figure 12. [S II]/Hα (S2H) ratio map of the Hourglass region. An enlargement of the central part is shown in the upper-right corner of the panel. The letters A, B and C refer to the regions described in the text (see Sections 3.7 and 3.8). The dashed-lined rectangular box defines the area shown in Fig. 15. The arrow indicates the direction to the O-type star 9 Sgr, located 4.12 arcmin from the finger-shaped molecular globule.

explained by considering normal photoionized gas filling the volume in front of the nebula. This gas shows a S2H flux ratio close to 0.05, and then reduces the contrast between the shock-excited features with higher values and the molecular cloud. As mentioned in Section 3.7, the dust associated with this foreground material could be responsible for most of the foreground extinction in the nebula.

Perhaps the most striking features in the [S II] and S2H images are three nebular knots located 40 arcsec to the south-east of Her 36, which appear to form one large structured bow shock for which the

Table 3. Equatorial coordinates of the new HH objects in the Hourglass nebula.

Object	α(J2000.0)	δ(J2000.0)	Comments
HH 867	18:03:36.77	−24:22:33.0	4 × 2.5 arcsec^2 ring, strong in [S II]
HH 868	18:03:36.00	−24:22:49.0	Three emission arcs, 6 arcsec in size
HH 869	18:03:35.69	−24:22:30.3	Strong [S II] knot
HH 870	18:03:41.44	−24:23:25.0	Three strong emission knots, 10 arcsec in size

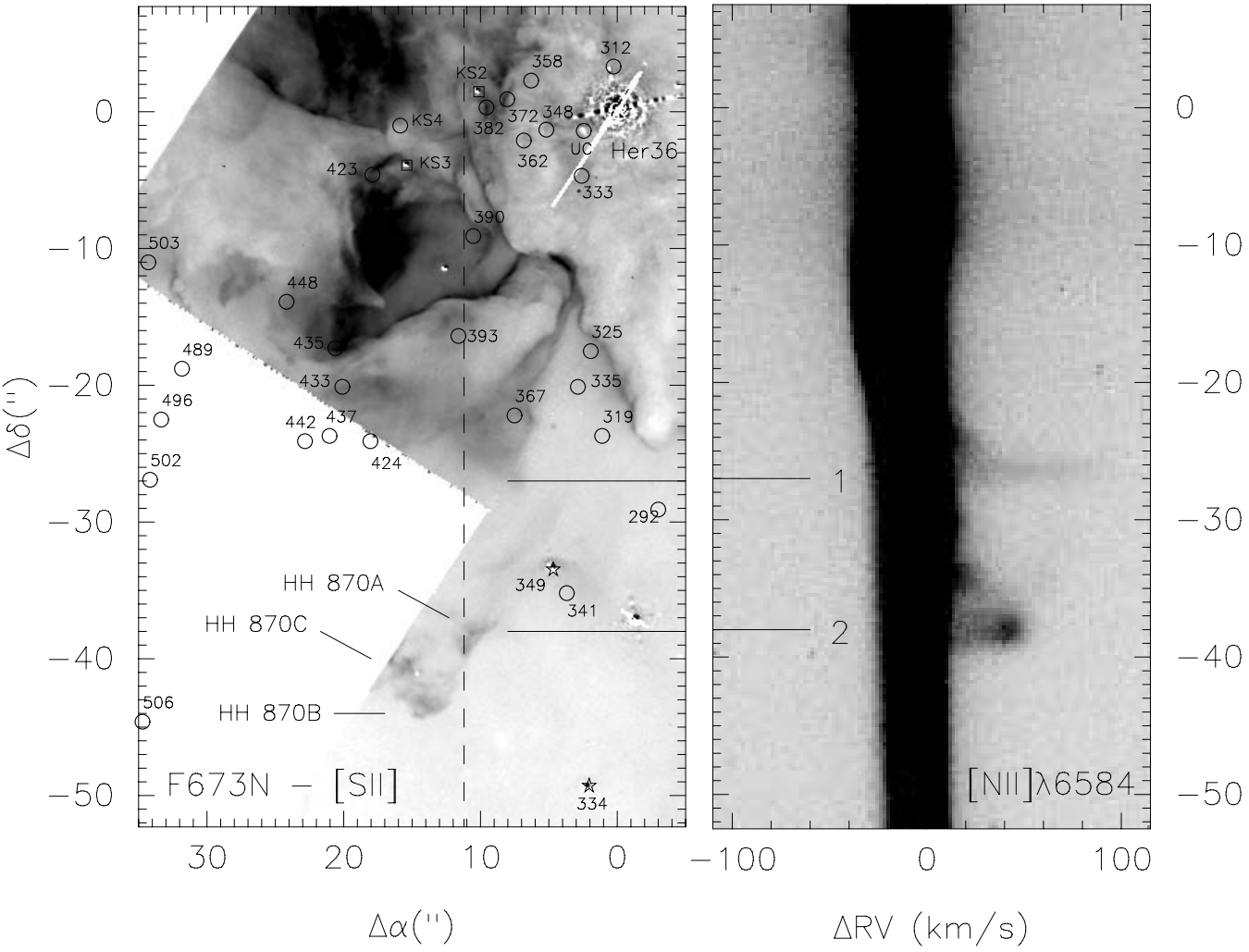

Figure 13. Right-hand panel: long-slit spectrum in the [N II] 6584-Å emission line obtained across the Hourglass nebula with the NTT. Left-hand panel: [S II] WFPC2 mosaic showing the location of the long-slit aperture (dashed line) and the infrared sources (circles). The stars indicate the position of the two sources showing bow shocks around them.

HH number HH 870 has been assigned in the HH catalogue.[3] Equatorial positions for this and the other new HH objects discovered in the Hourglass region are shown in Table 3. The morphological appearance of HH 870 is similar to the HH 203 and HH 204 objects in the Orion nebula (O'Dell et al. 1997). Its three flow components have been labelled as A, B and C in Fig. 13. The right-hand panel of this figure shows a long-slit spectrum in the [N II] 6584-Å emission line obtained across the Hourglass nebula with the NTT. The placement of the long-slit aperture has been plotted on the [S II] WFPC2 mosaic in the left-hand panel of the same figure. Two noticeable kinematic structures (labelled '1' and '2') are clearly observed. These velocity components are associated with nebular structures located at 25 arcsec (0.15 pc) and 37 arcsec (0.22 pc) from the middle point of the slit. Their receding velocities with respect to the H II region reach 80 km s^{-1} for feature '1' and 45 km s^{-1} for feature '2'. Feature '1' seems to originate in the gas located immediately to the south of a dusty finger-like structure whose head points directly to Her 36. Feature '2' is clearly associated with the flow component A of HH 870. It must be taken into account that the long-slit images were originally obtained with other scientific purposes, and so the

[3] HH catalogue numbers are assigned by B. Reipurth in order to correspond with the list of HH objects that he maintains.

position on the sky was chosen. It was a fortunate coincidence that the slit aperture crossed the western bow shock feature, but it is presumably not aligned along the jet axis. This could explain the undetection of the northern counterjet, although it also might be a result of the fact that the driving source is buried in the molecular cloud core. Both infrared sources 414 (KS 4) and 410 (KS 3) are located along the symmetry axis of the main bow shock component B of HH 870. As was remarked in Section 3.6, KS 4 is probably a Class I protostar and therefore a good candidate to be the driving source of this structure.

One-sided outflows are commonly observed emerging from dense cores in the photoionized medium: cf. HH 616 and HH 617 in S140 (Bally et al. 2002); HH 777 in IC 1396N (Reipurth et al. 2003). Additional evidence in favour that kinematic feature '2' (spatially associated with the feature HH 870A) is a bona fide bow shock is found in the very high [N II]/Hα (N2H) ratio derived from the long-slit spectra. Fig. 14 shows the superposition of the Hα and [N II] 6584-Å (scaled by 2) profiles along the position of feature '2'. The N2H ratio value is about 0.15 for the main emission component, but increases to about 0.7 for the radial velocity component at +45 km s^{-1}, reinforcing the idea that this feature is in fact shock-excited.

About 50 arcsec (0.3 pc) to the west of Her 36, we find another set of nebular structures which are also identified as new HH objects. Fig. 15 shows a portion of the WFPC2 Hα and [S II] mosaics and the S2H ratio map, where these interesting features have been labelled HH 867, HH 868 and HH 869 according to the numbers assigned in the HH catalogue.

The object HH 867 is a very intriguing elliptical ring, approximately 4 × 2.5 arcsec^2 in size (5000 × 3100 au). The ring is incomplete and presents strong emission in [S II] and much weaker emission in Hα, leading to a S2H ratio of about 0.11. A jet-like feature seems to cross axially the centre of the ring with a certain inclination angle respect to the ring plane. This candidate jet shows two main condensations with high S2H ratio: the first (S2H∼0.18) is placed toward the west of the ring, whereas the other (S2H∼0.11) is located on its eastern border. Furthermore, the jet seems to extend beyond the west end of the ring in a diffuse path of about 28 arcsec (0.17 pc), which can be mainly seen in the S2H ratio map. Near the apparent jet axis, there are two infrared excess sources, 32 (K_s = 13.04, J–H = 1.50, H–K = 1.00) and 11 (K_s = 15.73, J–H = 1.14, H–K = 1.25), which seem to be connected by a thin Hα filament. Source 11 coincides with the eastern jet condensation. Since both sources are candidates to be embedded YSOs, either of them might be the driving source of the jet feature.

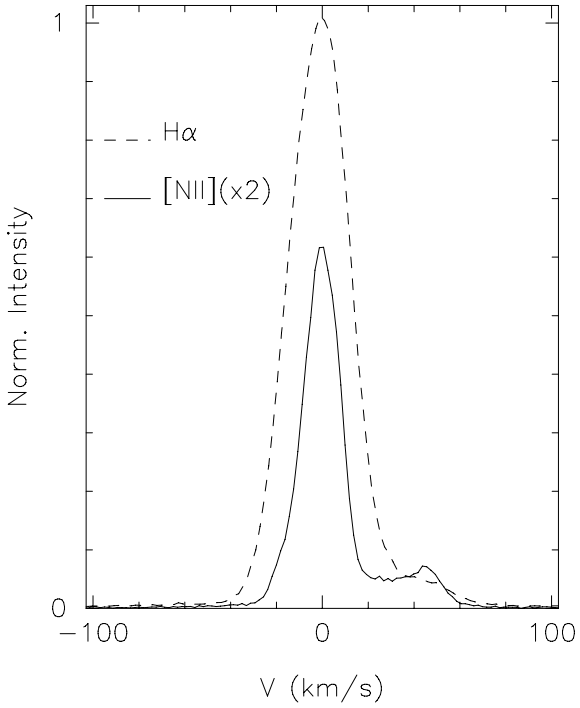

Figure 14. Superposition of the Hα and [N II] 6584-Å (scaled by 2) profiles along the position of feature '2' in Fig. 13.

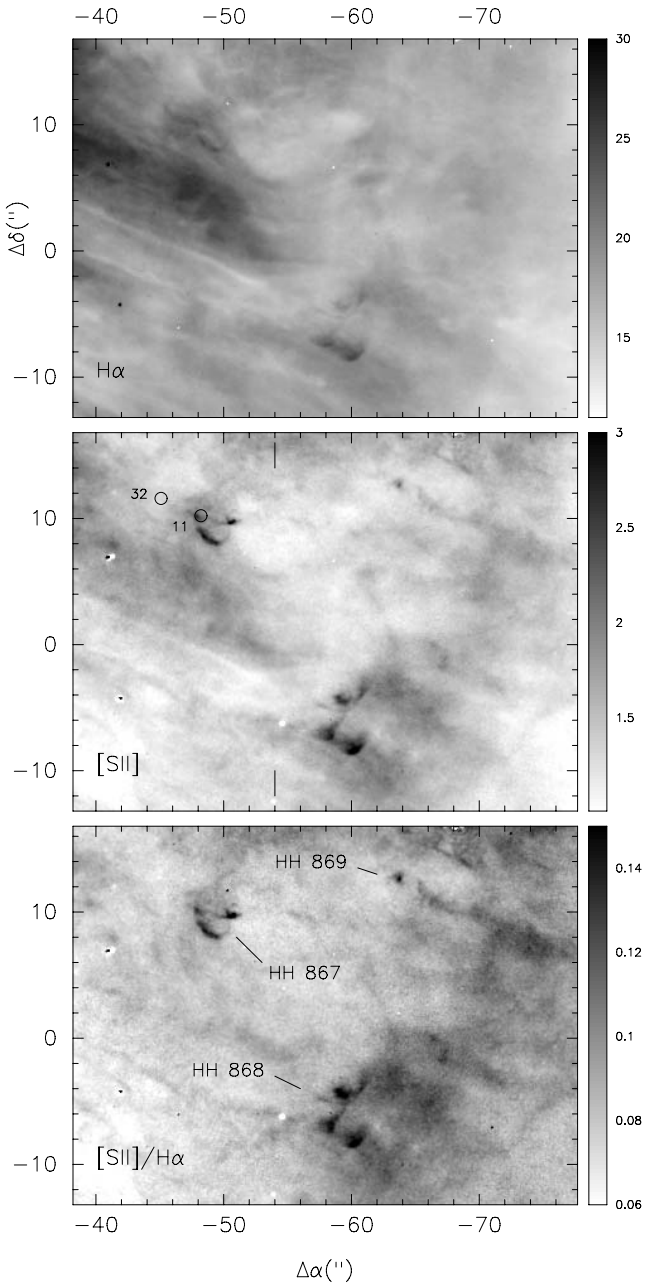

Figure 15. WFPC2 Hα and [S II] mosaics (top and middle panels) and S2H ratio map (bottom panel) showing three of the new HH objects identified in the Hourglass region (HH 867, HH 868 and HH 869) The infrared sources 32 and 11 are also marked with circles. For the top and middle panels, the surface brightness units are 10^{-16} erg cm^{-2} s^{-1} per WFC pixel.

HH 868, located about 20 arcsec to the south-east of HH 867, is an even larger structure (6 arcsec in size = 7500 au) composed by three nebular emission arcs. These bow shock features show high S2H ratio values (∼0.13) and they are undetectable in the Hα/Hβ map, which means that the extinction has foreground origin. The northern arc shows a bright [S II] condensation inside the bow shock, suggesting a reverse shock ('Mach disc'), indicative of the action of a faster jet overtaking cooled gas behind the preceding bow shock. Note that it seems very likely, based on the morphology of the flow components, that HH 867 and HH 868 form independent bow shocks in a single large flow coming from the upper left of the image.

A third HH object is found in Fig. 15. HH 869 is a bright [S II] condensation located 15 arcsec (19 000 au) to the west of HH 867, almost perpendicularly to the previously mentioned ring plane. This condensation is not appreciable in Hα emission, showing a S2H ratio value of ∼0.12. Our infrared survey does not reach this peculiar emission feature and the 2MASS catalogue does not show any infrared source close to this location. A diffuse filament seems to develop from HH 869, grow in the south-west direction and intersect the filament coming from HH 867. Bally et al. (2002) describe the breakout in an ionized medium of a jet arising inside the molecular cloud. They found that the wall of the molecular cloud shows arcs with enhanced [S II] emission where the jet appears. In this way, we should also bear in mind the hypothesis that the ring of HH 867 represents the point in the molecular cloud where a jet arising in (or around) Her 36 emerges, because the normal direction to the ring points directly to that star. Furthermore, the HH 869 feature is placed along the line joining the ring and Her 36.

Chakraborty & Anandarao (1997, 1999) performed Fabry–Perot observations of the Hourglass region in the [N II] 6583-Å and [O III] 5007-Å emission lines. They found high expansion velocities up to 50 km s^{-1}, which they interpreted as indicative of Champagne flows. Unfortunately, the area observed by these authors does not reach the location of the outflow HH 870. Nevertheless, a careful inspection of their plots suggests the possibility that some of the high-velocity features observed in their spectral line profiles may represent the contribution of collimated outflows to the general turbulent motion. For example, among the line profiles shown in fig. 2 of Chakraborty & Anandarao (1997), there is a high velocity component of −50 km s^{-1}, which appears very prominent at position angle 190°, 20 arcsec from Her 36 (fig. 2h) but it is not observed at position angle 175°, 12 arcsec from this star (fig. 2f). This type of small-scale variation in the structure of the velocity field may indicate the existence of collimated outflows.

Located 30 arcsec (0.18 pc) to the north-west of Her 36, source 156 (SCB 1040) is a remarkable object which has already been suggested as a pre-main-sequence candidate from its optical colours in *HST* data by Sung et al. (2000). Its Hα image shows extended emission (0.5 arcsec in size) and reveals a chain of nebular emission features extending 10 arcsec to the south, which clearly resembles the one-sided jets detected in the Orion nebula (Bally, O'Dell & McCaughrean 2000).

About 7.5 arcsec (9400 au) to the south of source 156 is source 144, which shows an intense and very elongated Hα emission. This star has infrared colours similar to T Tauri stars (J–H = 1.36, H–K_s = 0.82). Additionally, its K_s magnitude of 10.14 corresponds to the same brightness as T Tauri itself (J–H = 1.02, H–K_s = 0.91 and K_s = 5.33, according to the 2MASS Second Incremental Data Release; Cutri et al. 2000), if moved from its location in the Taurus T association (140 pc) to the distance of M8 (1300 pc).

A rich clustering of faint infrared sources (369, 374, 497, 320, 370) is found 35 arcsec (0.2 pc) to the north of Her 36, close to bright filaments facing 9 Sgr. These filaments are part of the PDR of the molecular core detected in CO (see Fig. 8).

The central part of the Hourglass nebula shows an incredible complex structure which will be better described in a subsequent paper. We remark here a large dust pillar orientated to Her 36 in the south-east–north-west direction, which is observed as an extinction feature against the nebular background. Its very bright rimmed head indicates that it is presumably illuminated on its far side, and so is somewhat in front of Her 36. The projected distance between the head of the pillar and the star is 11 arcsec (0.07 pc). Our K_s-band image reveals a bright stellar infrared source (347) located in the tip of this finger, resembling those found in the dense knots of 30 Doradus by Walborn et al. (1999). Source 347 has no optical counterpart and its near-infrared colours are typical of a highly reddened early-type star (J–H = 1.72, H–K_s = 1.05).

In the southern region of the field, the WFPC2 images reveal another interesting dust structure, which might probably be an externally ionized molecular globule similar to that found in the core of the Carina nebula by Smith, Barbá & Walborn (2004). This molecular globule, located ∼105 arcsec to the south-west of the Hourglass, has also a shape resembling a human finger that points toward its likely source of ionizing photons. Curiously, the finger does not point to Her 36 but to the O4 V(f)-type star 9 Sgr. While the finger is seen only as a silhouette against a brighter background in Hα, its surface is very bright in [S II], which is especially clear from the S2H ratio map in Fig. 12. Although most of this structure is out of the field of view of our infrared images, a very bright infrared stellar source is noticeable in the summit of the pillar. The 2MASS archive data reveal the presence of a highly reddened object at this location (J = 14.603, J–H = 3.018, H–K_s = 1.502).

Finally, we have identified two large bow shocks surrounding young stars whose near-infrared colours are typical of reddened T Tauri stars: sources 349 (J–H = 1.25, H–K_s = 0.64) and 334 (J–H = 1.44, H–K_s = 0.84). These objects are marked with stars in Fig. 13. It is interesting to note that, while source 334 is a single star in *HST* images, it is observed as a double star with components separated by 0.5 arcsec in our infrared images. The eastern component is not detected in the optical images, but it is brighter than its companion in the infrared. This object seems to be a resolved binary with components affected by a different degree of extinction.

The bow shocks detected in sources 349 and 334 are seen as arcs consisting in bright Hα emission and facing Her 36. In both cases, they are concave toward the corresponding infrared source and convex toward Her 36. The bow shock around star 349 is brighter than that around star 334. Their morphologies resemble strongly the hyperbolic bow shock around the T Tauri star LL Ori (Bally et al. 2000; Bally & Reipurth 2001). Thus, these bow shocks are candidates to be wind–wind collision fronts.

In summary, the morphological analysis of the *HST* images of the Hourglass region reveals that the nebula has a complex structure, showing dozens of features that closely resemble those observed in other star-forming regions (for example, M42, M16 and NGC 3372). However, almost nothing is known yet about the proper motion and radial velocity of these objects, so it is premature to draw any conclusions about these objects here. In a forthcoming paper, we will discuss optical spectroscopy recently obtained using the Boller and Chivens Spectrograph on the 6.5-m Magellan I telescope at LCO, which will undoubtedly contribute to the unveiling of their true nature.

4 SUMMARY AND CONCLUSIONS

We have obtained near-infrared JHK_s images of the Hourglass nebula in M8. These data were complemented with *HST* images and long-slit spectroscopy retrieved from on-line data bases. The main results can be summarized as follows.

We used the recently developed numerical code CHORIZOS to obtain a new estimate for the distance to the Hourglass region. Using optical and infrared photometry from this work and from literature for a group of early-type stars around Her 36 (including this star), we derived a distance modulus of 10.5 (1.25 kpc). This value is sensibly smaller than the 11.25 previously accepted for the region, but it is in excellent agreement with the last determination for NGC 6530 by Prisinzano et al. (2005).

Our infrared images confirm the existence of a very young stellar cluster around the massive O-type star Her 36. We have detected almost 100 sources with colours indicative of intrinsic infrared excess emission, which appear as prime candidates to be T Tauri and Herbig Ae/Be stars. These objects are not uniformly distributed in the region, but they extend along the molecular core, mostly concentrated near the two most intense peaks of the CO distribution (White et al. 1997). The large fraction of infrared excess sources (over 70 per cent in the central part of the field) along with the evidence of outflow activity from Her 36 (Burton 2002) suggest the stellar population within the cluster must be extremely young ($\sim 10^6$ yr).

By comparing the JHK_s photometric diagrams of the Hourglass and a 2MASS control field, we have found that a significant fraction of the stars observed toward M8 may be red giants belonging to the galactic inner disc and bulge. Based on the method described by Lada et al. (1994), we have used the positions and near-infrared colour excess estimates of over 400 background field giants to directly measure the extinction through the molecular cloud, finding a strong correlation with the distribution of molecular material.

Archival *HST* emission-line images reveal a variety of ongoing star formation features in the core of M8. Several of the candidate YSOs detected here seem to be associated with structures similar to those observed in other star-forming regions such as M16 and M42, i.e. proplyds, jets, dense knots, molecular globules and bow shocks. Furthermore, four HH objects have been detected for the first time in the region (HH 867, HH 868, HH 869 and HH 870). A long-slit spectrum in the [N II] 6584-Å emission line obtained across the Hourglass nebula with the NTT and retrieved from the ESO Archive Facility confirmed the identification of HH 870, providing the first direct evidence of active star formation by accretion in M8. In order to understand better the nature of some of the rest of the objects, we have obtained optical spectroscopy with the 6.5-m Magellan telescope, which will be analysed in a future paper.

ACKNOWLEDGMENTS

This publication makes use of data products from the 2MASS, which is a joint project of the University of Massachusetts and the Infrared Processing and Analysis Center/California Institute of Technology, funded by the National Aeronautics and Space Administration and the National Science Foundation. This research has made use of Aladin and the Simbad data base, operated at CDS, Strasbourg, France.

Financial support from 'Fondo de Publicaciones de la Dirección de Investigación de la Universidad de La Serena (Chile)' and from FONDECYT No. 1050052 is acknowledged by RHB. Also, MR acknowledges to the Center for Astrophysics (FONDAP No. 1501003, Chile). JIA thanks the Departamento de Física of Universidad de La Serena for the use of their facilities and the warmest hospitality. Also, the authors gratefully thank the staff at LCO for kind hospitality during the observing run, and Bo Reipurth for his advice about the classification of HH objects.

REFERENCES

Allen D. A., 1986, MNRAS, 219, 35
Bally J., Reipurth B., 2001, ApJ, 546, 299
Bally J., O'Dell C. R., McCaughrean M. J., 2000, AJ, 119, 2919
Bally J., Reipurth B., Walawender J., Armond T., 2002, AJ, 124, 2152
Bica E., Dutra C. M., Soares J., Barbuy B., 2003, A&A, 404, 223
Burton M. G., 2002, PASA, 19, 260
Cardelli J. A., Clayton G. C., Mathis J. S., 1989, ApJ, 345, 245
Chakraborty A., Anandarao B. G., 1997, AJ, 114, 1576
Chakraborty A., Anandarao B. G., 1999, A&A, 346, 947
Chen Y. et al., 2003, A&A, 401, 185
Cutri R. M. et al., 2000, Explanatory Supplement to the 2MASS Second Incremental Data Release. Infrared Processing and Analysis Center (IPAC), Pasadena
Jones T. J., Hyland A. R., 1980, MNRAS, 192, 359
Kenyon S. J., Hartmann L., 1995, ApJS, 101, 117
Kilambi G. C., 1977, MNRAS, 178, 423
Koornneef J., 1983, A&A, 128, 84
Lada C. J., Lada E. A., Clemens D. P., Bally J., 1994, ApJ, 429, 694
Lada C. J., Alves J., Lada E. A. J., 1996, AJ, 111, 1964
Laidler V. et al., 2005, Synphot User's Guide, version 5.0. STScI, Baltimore
Lanz T., Hubeny I., 2003, ApJS, 146, 417
Lightfoot J. F. et al., 1984, MNRAS, 208, 197
Maíz-Apellániz J., 2004, PASP, 116, 859
Maíz-Apellániz J., 2006, in Livio M., Brown T. M., eds, The Local Group as an Astrophysical Laboratory, Space Telescope Science Institute Symposium Series No. 17. Cambridge Univ. Press, Cambridge, in press
Maíz-Apellániz J., Walborn N. R., Galué H. A., Wei L. H., 2004a, ApJS, 151, 103
Maíz-Apellániz J., Pérez E., Mas-HessePérez J. M., 2004b, AJ, 128, 1196
Martin P. G., Whittet D. C. B., 1990, ApJ, 357, 113
Mason B. D., Gies D. R., Hartkopf W. I., Bagnuolo W. G. Jr, Brummelaar T. T., McAlister H. A., 1998, AJ, 115, 821
Meyer M. R., Calvet N., Hillenbrand L. A., 1997, AJ, 114, 288
O'Dell C. R., Doi T., 1999, PASP, 111, 1316
O'Dell C. R., Hartigan P., Lane W. M., Wong S. K., Burton M. G., Raymond J., Axon D. J., 1997, AJ, 114, 730
Osterbrock D. E., 1989, Astrophysics of Gaseous Nebulae and Active Galactic Nuclei. University Science Books, Mill Valley, CA
Persson S. E. et al., 1992, PASP, 104, 204
Persson S. E. et al., 1998, AJ, 116, 2475
Prisinzano L., Damiani F., Micela G., Sciortino S., 2005, A&A, 430, 941
Rauw G., Nazé Y., Gosset E., Stevens I. R., Blomme R., Corcoran M. F., Pittard J. M., Runacres M. C., 2002, A&A, 395, 499
Reipurth B., Bally J., 2001, ARA&A, 39, 403
Reipurth B., Armond T., Raga A., Bally J., 2003, ApJ, 593, L47
Rieke G. H., Lebofsky M. J., 1985, ApJ, 288, 618
Sagar R., Joshi U. C., 1978, MNRAS, 184, 467
Smith N., Barbá R. H., Walborn N. R., 2004, MNRAS, 351, 1457
Stecklum B., Henning T., Eckart A., Howell R. R., Hoare M. G., 1995, ApJ, 445, 153
Stecklum B., Henning T., Feldt M., Hayward T. L., Hoare M. G., Hofner P., Richter S., 1998, AJ, 115, 767
Sung H., Chun M., Bessell M., 2000, AJ, 120, 333
van Altena W. F., Jones B. F., 1972, A&A, 20, 425
van den Ancker M. E., Thé P. S., Feinstein A., Vázquez R. A., de Winter D., Pérez M. R., 1997, AAS, 123, 63
Walborn N. R., 1972, AJ, 77, 312
Walborn N. R., 1973, AJ, 78, 1067

Table 4. Infrared sources in the field of the Hourglass nebula. A full copy of this table is available as supplementary material in the on-line version of the journal.

ABMMR no. (1)	α (J2000.0) (2)	δ (J2000.0) (3)	J (4)	$\sigma(J)$ (5)	H (6)	$\sigma(H)$ (7)	K_s (8)	$\sigma(K_s)$ (9)	J–H (10)	H–K_s (11)	Comment (12)
1	18:03:36.60	−24:22:54.4	18.665	0.089	15.774	0.106	13.978	0.017	2.891	1.796	
2	18:03:36.61	−24:22:29.4	19.012	0.142	15.63	0.1	13.658	0.014	3.382	1.972	
3	18:03:36.66	−24:23:48.0	18.598	0.107	16.2	0.056	14.802	0.033	2.398	1.398	
4	18:03:36.69	−24:21:53.8	–	–	–	–	16.02	0.048	–	–	
5	18:03:36.70	−24:22:52.8	20.002	0.404	16.465	0.074	15.532	0.059	3.537	0.933	
6	18:03:36.71	−24:23:06.2	18.439	0.082	16.218	0.023	15.125	0.03	2.221	1.093	
7	18:03:36.72	−24:21:43.7	18.303	0.136	15.73	0.08	14.683	0.036	2.573	1.047	
8	18:03:36.74	−24:23:10.7	18.734	0.19	16.198	0.038	14.901	0.038	2.536	1.297	
9	18:03:36.75	−24:23:07.9	20.463	0.488	17.416	0.077	16.551	0.07	3.047	0.865	
10	18:03:36.77	−24:23:16.2	19.36	0.289	17.559	0.104	16.8	0.115	1.801	0.759	

Walborn N. R., Barbá R. H., Brandner W., Rubio M., Grebel E. K., Probst R. G., 1999, AJ, 117, 225
Walborn N. R., Maíz-Apellániz J., Barbá R. H., 2002, AJ, 124, 1601
Wang H., Yang J., Wang M., Yan J., 2003, AJ, 125, 842
Whittet D. C. B., Martin P. G., Fitzpatrick E. L., Massa D., 1993, ApJ, 408, 573
White G. J., Tothill N. F. H., Matthews H. E., McCutcheon W. H., Huldtgren M., McCaughrean M. J., 1997, A&A, 323, 529
Woodward C. E., Pipher J. L., Helfer H. L., Forrest W. J., 1990, ApJ, 365, 252
Zombeck M. V., 1990, Handbook of Space Astronomy and Astrophysics, 2nd edn. Cambridge Univ. Press, Cambridge

SUPPLEMENTARY MATERIAL

The following supplementary material is available for this article on-line:

Table 4. Infrared sources in the field of the Hourglass nebula.

This material is available as part of the on-line article from http:www.blackwell-synergy.com.

This paper has been typeset from a TEX/LATEX file prepared by the author.